ABSTRACT

Title of Document: SYNTHESIS, CHARACTERIZATION, AND BIO-CONJUGATION OF SILICON NANOCRYSTAL

Jonghoon Choi, M.S., 2006

Directed By: Associate Professor, Nam Sun Wang, Department of Chemical and Biomolecular Engineering

Bulk silicon is unable to emit fluorescence because of its indirect band gap nature. However, it has been reported that nano-structured silicon can be fluorescent when properly excited. Silicon nanocrystals (SN) have gathered scientific attention not only because of their uncertain fluorescence origin, but also because of their advantages over fluorescent dyes. This thesis summarizes studies on the synthesis, characterization and bio applications of fluorescent SN. Size control of SN provided size dependent tuning of the fluorescence. Higher quantum yield and narrower size distribution of SN have been achieved. HrTEM, SANS, light scattering, photoluminescence and optical transmission spectroscopy on the size measurements of SN helped determine the average size accurately. Fuctionalization of surface prepares silicon nanocrystals as a platform for bio conjugating applications.

SYNTHESIS, CHARATERIZATION, AND BIO-CONJUGATION OF SILICON NANOCRYSTAL

By

Jonghoon Choi.

Thesis submitted to the Faculty of the Graduate School of the
University of Maryland, College Park, in partial fulfillment
of the requirements for the degree of
Master of Science
2006

Advisory Committee:
Associate Professor Nam Sun Wang, Chair
Professor Kyu Yong Choi
Assistant Professor Srinivasa R. Raghavan
Dr. Vytautas Reipa

dedicated to my be loved family, Sena, and Jesus Christ

Acknowledgements

Life is a challenge! At least, last two years of my life verifies that maxim. Every day and every moment that I have lived and studied in United States was a real challenge for me. Sometimes, I did almost give up studying and just wanted to go back home. In the other times, I truly enjoyed new friends and every single of new thing I had to face. While I prepare my thesis, it has been a great pleasure of me to look back those past two years and remember the days that I cried and laughed. I truly believe that without the support of my good friends, colleagues, loved ones and Jesus Christ, I couldn't have made it through. I would like to acknowledge all those loved ones here and thank you all for trusting and supporting me.

I'd like to thank my advisor at University of Maryland, Dr. Nam Sun Wang for all his advice and mentoring during my study and life in the US. I was able to learn a lot in many respects from his always warm and friendly attitude toward other people. I'd like to acknowledge my other advisor at NIST, Dr. Vytas Reipa for all his invaluable support, advice and discussions we had. I am really lucky to have those two very good persons as advisors.

I'd like to thank all my colleagues at NIST for all of their support and help. I am getting a lot of experience everyday working on theses projects and knowledge that I cannot learn from a textbook.

I also want to acknowledge my lab mates at the University of Maryland. Sharing ideas and spending time together with you guys is always full of fun!

All my Korean friends at school and NIST, I would like to appreciate you all for our good memories. I am sure we will have more great moments in the following years.

I'd like to thank you KBS and KUMC brothers and sisters for sharing life together and being each other's light house in our lives. My be loved Family in Korea, I do and will always love you all. And my one and only love Sena, I thank you and thank God for our beautiful love. Finally, I thank Jesus Christ for his love and being the lord of our lives all the time.

Table of Contents

List of Tables

List of Figures

Figure 3.1 TEM images of the Si nanocrystals prior to dissolution. Right panel shows a high-resolution image of an 8 nm dia particle with visible lattice planes.

Figure 3.2 Si particle suspensions in methanol. (Top) Absorbance of freshly prepared particles (solid line) decomposed into scattering (dotted line) and absorbing (dashed line) components. (Bottom) Absorbance evolution after the introduction of the 10 micro liters of 10:1 HF/HNO_3 mixture and exposure to UV light. Insert compares the 320 nm absorbance decay rates with and without UV exposure (full and open circles respectively). T=293K.

Figure 3.3 Si particle size distribution, estimated using from dynamic light scattering measurement. Full bars represent suspension following Si wafer sonication in methanol, shaded bars- after 30 min photo-catalyzed etch in HF/HNO3 mixture.

Figure 3.4 Si particle photoluminescence recorded during various stages of photo-catalyzed dissolution in the acid mixture. $\lambda_{exc} = 360$ nm.

Figure 3.5 Multicolor photoluminescence pattern in the stationary Si nanoparticle suspension during the UV catalyzed acid dissolution. Sample cell was illuminated at 340 nm through the bottom cell window.

Figure 3.6 Photoluminescence spectra recorded during photo-catalyzed Si nanoparticle dissolution: 1- prior to acid introduction, 2- 30min after acid addition, 3- 50min, 4- 80min, 5- 110min, 6- 130min, 7- 170min, 8- 200min.

Figure 3.7 Initial Si nanocrystal size distribution function used in the dissolution model. Inset shows the suspension photoluminescence profile. λ_{exc} = 360nm.

Figure 3.8 Simulated distribution functions during Si nanoparticle suspension dissolution in acid mixture. Equation (12) input parameters $N_0 = 10^4$, d* = 5, $\alpha = 0.2$, $\sigma_2 = 1.5$ and $d_r = 5$. 1- Initial distribution, 2 -17min after acid addition, 3 - 50 min, 4- 100 min, 5- 200 min.

Figure 3.9. Photoluminescence bandwidth at half maximum during the photo-catalyzed dissolution reaction of Si nanocrystal suspension in HF/HNO_3 mixture. Black dots with solid trend line is a FWHH with UV supported experiment. White dots with dotted trend line is a FWHH changes without UV support.

Figure 4.1. Model fitting on the low-q region of scattering cross section versus scattering wave vector obtained from SANS measurement. Lognormal poly sphere model has been implemented with predicted parameters from Guinier approximation.

Figure 4.2 Size distribution curve from the model fitting of SANS data on the low-q range ($0.001<q<0.04$).

Figure 6.2 Detailed chemistry of ATFB crossliker connecting carbo-hydro terminated silicon surface to the amine containing bio molecule. (Image courtesy of Invitrogen, CA)

Figure 6.3 Stained gel after the native gel eletrophoresis. 200V, 2 hour elution, and the mobile buffer is Tris-HCl, pH 6.8.

Chapter 1: Silicon nanocrystals

1.1 Objective of study

Silicon nanocrystals whose sizes are below 5 nm in diameter are fluorescent under UV excitation. They shine in every spectral range of color according to their sizes. I am interested in a macro synthesis of the silicon nanocrystals, tuning of their fluorescence by controlling the sizes and homogeneity, characterizing spectroscopic properties of silicon nanocyrstals, chemically modifying particle's surface, and utilizing theses nanocrystals as a fluorophore in biological applications.

1.2 Quantum dots today

Because of the superior photo stability, narrow range of emission, broad excitation wavelength, multiple possibilities of modification, quantum dots have gathered much attention from engineering and scientists who are interested in bio markers, sensors or drug targeting [1]~[8]. Commercially available binary quantum dots from Qdot [Qdot Company] have been successfully applied for above purposes during the last 10 years and reported in a vast number of literatures. Although quantum dots are useful as a tagging material, they also have several disadvantages. First and the most serious demerits of binary quantum dot is that it is toxic to cells. Most popular components of binary quantum dots are cadmium / serenide which are deleterious to cells. Because of the intrinsic toxicity of binary quantum dot, very thick surface coating is required. The final size of quantum dot is almost twice as thick as

the initial core size and hinders the applications of qdots in a cell. Figure 1.1 shows the general structure of binary quantum dots reported by Qdot Company. Another drawback of binary quantum dot is its blinking behavior when a single binary qdot is observed with confocal fluorescent microscope [9][10]. Its blinking behavior hinders the tracking of qdot targeted bio molecule in a bio system.

1.3 Promising aspects of silicon nanocrystals

Because of drawbacks of binary quantum dots, silicon nanocrystal has been studied to overcome the demerits of commercially available qdots and be used as a substituting fluorophore with traditional organic dyes. Silicon nanocrystal's superiorities as a fluorophore are summarized in Table 1.1. Silicon is basically non toxic to cells so that it does not require a thick surface coating to prevent exposure of core to the environment. Therefore, its average size remains close to its core size.

	Silicon Nanocrystal	Binary Quantum dot	Organic dye
Average Size	1~4 nm (in dimeter)	10~20 nm (in diameter)	0.5~10 nm
Quantum Yield	< 60 %, [11]	>50 %	>90 %
Photostability	> 6 month	No data	1 day
Blinking	No data	Micro second [9][10]	No data

Table 1.1 Comparison of characteristic properties of Silicon nanocrystal with binary Qdots and traditional organic dyes.

Figure 1.2 compares the size of silicon nanocrystal and binary qdots with various materials. Because of its smaller average sizes (<5 nm in dia.), it can penetrate cell membrane or cell nucleus [2] to use qdots as a bio tagging material inside a bio system. Another important characteristic of silicon nanocrystal is that its blinking

behavior is reported to be less problematic. Si nanocrystal is at keeping track of bio conjugates in a system.

1.4 History and principles of silicon nanocrystal fluorescence.

Bulk Si is a rather inefficient light emitter due to the indirect-band gap electronic structure, requiring a phonon to balance electron momentum during inter-band transition. Fortunately, momentum requirements are relaxed in 1-5 nm dia Si crystals as a result of so-called quantum confinement effects that allows for efficient light emission. Silicon nanocrystals are increasingly studied due to their unique physicochemical properties [12] including photoluminescence in the visible part of the electromagnetic spectrum. Significant progress in studying related phenomena in II-VI compound semiconductor quantum dots and successful photonic applications [13][14] have re-energized interests in nanoscale Si, a phenomenon discovered back in the 1950's [15]. First observation of fluorescence from silicon was performed by Lehigh Canham in 1980s. Photoluminescent SN, along with C and SiC based nanoparticles, are considered bio-inert [16] and could lead to the development of smaller biocompatible probes [17][18] that are potentially will facilitate their use in biomedical field. Moreover, SN surface is open to various chemical functionalizations thus offering numerous stabilization and bioconjugation options [19].

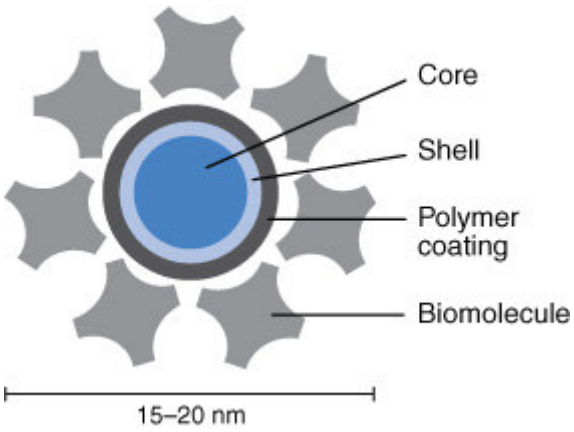

Fig 1.1 Drawing of typical commercially available binary quantum dot. Image courtesy of Invitrogen Co.

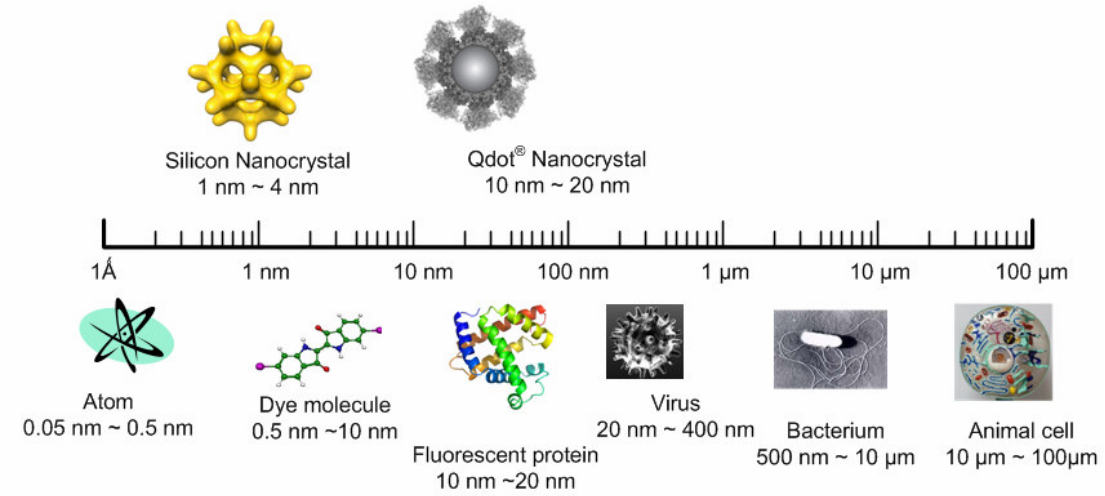

Fig 1.2 Comparison of sizes among silicon nanocrystal and Qdot nanocrystal with other materials. Image courtesy of Invitrogen Co.

1.5 Studies of synthsizing Si nanocrystal

Si nanocrystal preparation methods in general are more complicated than the well-established protocols for the II-VI compound based nanoparticles. Published procedures, including chemical synthesis [20], silane chemical [21] or electrochemical [22] reduction, laser assisted pyrolysis [23] and wet Si wafer etching in HF [24], provide milligram quantities of size dispersed Si nanocrystal. A rather straightforward procedure of the electrochemical Si wafer etching [17][24] is based on protocols developed for obtaining nano-porous Si [25]. Anodic wafer etching is followed by sonication that partially crumbles porous Si film, resulting in a nano-particle suspension [17]. Immediately after etching, particle surface is hydrogen atom passivated and can be oxidized or substituted by a variety of organic groups using post-etching functionalization [19]. Typically particles of various sizes and shapes are produced during such procedures represented by a wide range of physicochemical properties. Narrow particle size distribution is desirable in most applications due to the strong size dependence of the particle electronic structure when particle diameter is less than 5 nm [26]. Therefore techniques to homogenize Si nanoparticle preparations using centrifugation [26], selective precipitation [27] size exclusion chromatography and capillary electrophoresis [28], are actively pursued.

1.6 Structure of thesis

Studies on synthesis, characterizations and applications of silicon nanocrystal are covered in following chapters. In Chapter 2, method of producing 1~4 nm size Si nanoparticles from the anodic etching of Si wafer is depicted. Studies on narrowing of size distribution and tuning of Si nanocrystal's fluorescence are described in Chapter

3. Various approaches to determine average sizes of produced Si nanocrystal are followed in Chapter 4. Studies on a surface functionalization of Si nanocrystal are described in Chapter 5. Chapter 6 describes the bio conjugation of Si nanocrystals. And finally in Chapter 7, conclusions and future works are summarized. All studies and discussions in these chapters help understand the nature of silicon nanocrystal and direct to possible applications in the future.

1.7 References

1. Medintz, I. L; Uyeda, H. T.; Goldman E. R.; Mattoussi H. "Quantum dot bioconjugates for imaging, labelling and sensing", *Nature Materials* **2005**, *4*, 435-446.
2. Clarke, S. J.; Hollmann C. A.; Zhang, Z.; Suffern, D.; Bradforth, S. E.; Dimitrijevic, N. M.; Minarik, W. G.; Nadeau, J. L. "Photophysics of dopamine-modified quantum dots and effects on biological systems", *Nature Materials* **2006**, *5*, 409-417.
3. Sun, B.; Marx, E.; Greenham, N. C. "Photovoltaic Devices Using Blends of Branched CdSe Nanoparticles and Conjugated Polymers", *Nano Lett.* **2003**, *3*, 961-963.
4. Watt, A.; Thomsen, E.; Meredith, P.; Rubinsztein-Dunlop, H. "A new approach to the synthesis of conjugated polymer–nanocrystal composites for heterojunction optoelectronics", *Chem. Commun.* **2004,** 2334-2335.
5. Larson, D. R.; Zipfel, W. R.; Williams, R. M.; Clark, S. W.; Bruchez, M. P.; Wise, F. W.; Webb, W. W.; "Water-Soluble Quantum Dots for Multiphoton Fluorescence Imaging in Vivo", *Science* **2003**, *300*, 1434-1436.

6. Imamoglu, A.; Awschalom, D. D.; Burkard, G.; DiVincenzo, D. P.; Loss, D.; Sherwin, M.; Small, A. "Quantum Information Processing Using Quantum Dot Spins and Cavity QED", *Phys. Rev. Lett.* **1999***, 83*, 4204-4207.
7. Redl, F. X.; Cho, K. S.; Murray, C. B.; O'Brien, S. "Three-dimensional binary superlattices of magnetic nanocrystals and semiconductor quantum dots", *Nature* **2003**, *423***,** 968-971.
8. Haremza, J. M.; Hahn, M. A.; Krauss, T. D.; Chen, S.; Calcines, J. "Attachment of Single CdSe Nanocrystals to Individual Single-Walled Carbon Nanotubes", *Nano Lett.* **2002**, *2*, 1253-1258.
9. Korberling, F.; Mews, A.; Basche, T. "Oxygen-Induced Blinking of Single CdSe Nanocrystals", *Advanced Materials* **2001**, *13*, 672-676.
10. Yao, J.; Larson, D. R.; Vishwasrao, H. D.; Zipfel, W. R.; Webb W. W.; "Blinking and nonradiant dark fraction of water-soluble quantum dots in aqueous solution", *Proc. of Nat. Aca. of Sci. of USA* **2005**, *102*, 14284-14289.
11. Choi, J.; Wang, N. S.; Reipa, V.; *Langmuir*, in revision.
12. Cullis, A. G.; Canham, L. T.; Calcott, D. J.; "The structural and luminescence properties of porous silicon", *J. Appl. Phys.* **1997**, *82*, 909-965.
13. Trindade, T.; O'Brien, P.; Pickett, N.L.; "Nanocrystalline Semiconductors: Synthesis, Properties, and Perspectives", *Chem. Mater.* **2001**, *13*, 3843-3858.
14. Michalet, X.; Pinaud, F.F.; Bentolila, L.A.; Tsay, J.M.; Doose, S.; Li, J.J.; Sundaresan, G.; Wu, A.M.; Gambhir, S.S.; Weiss, S.; "Quantum Dots for Live Cells, in Vivo Imaging, and Diagnostics", *Science* **2005**, *307*, 538-544.
15. Uhlir, A.; *Bell Syst. Tech. J.* "Electrolytic shaping of germanium and silicon",

1956, *35*, 333-347.

16. Reboredo, F.A.; Galli, G.; "Theory of Alkyl-Terminated Silicon Quantum Dots", *J. Phys. Chem. B.* **2005**, *109*, 1072-1078.
17. Wang, L.; Reipa, V.; Blasic, J. "Silicon Nanoparticles as a Luminescent Label to DNA", *Bioconjugate Chem.* **2004**, *15*, 409-412.
18. Ding, z.; Quinn, M. B.; Haram, A. K.; Pell, L. E.; Korgel, B. A.; Bard, A. L. "Electrochemistry and Electrogenerated Chemiluminescence from Silicon Nanocrystal Quantum Dots", *Science* **2002**, *296*, 1293-1297.
19. Buriak, J.M.; "Organometallic Chemistry on Silicon and Germanium Surfaces", *Chem. Rev.* **2002**, *102*, 1271-1308.
20. Bley, R.A.; Kauzlarich, S.M.; "A Low-Temperature Solution Phase Route for the Synthesis of Silicon Nanoclusters", *J. Am. Chem. Soc.* **1996**, *118*, 12461-12462.
21. Heath, J.R.; "A Liquid-Solution-Phase Synthesis of Crystalline Silicon", *Science* **1992**, *258*, 1131-1133.
22. Aihara, S.; Ishii, R.; Fukuhara, M.; Kamata, N.; Terunuma, D.; Hirano, Y.; Saito, N.; Aramata, M.; Kashimura, S.; "Electroreductive synthesis and optical characterization of silicon nanoparticles", *J. Non-Cryst. Sol.* **2001**, *296*, 135-138.
23. Hua, F.; Swihart, M. T.; Ruckenstein, E. "Efficient Surface Grafting of Luminescent Silicon Quantum Dots by Photoinitiated Hydrosilylation", *Langmuir* **2005**, *21*, 6054-6062.
24. Yamani, Z.; Ashhab, S.; Nayfeh, A.; Thompson, W. H.; Nayfeh, M. "Red to green rainbow photoluminescence from unoxidized silicon nanocrystallites", *J. Appl. Phys.* **1998**, *83*, 3929-3931.

25. Jung, K. H.; Shih, S.; Hsieh, T. Y.; Kwong, D. L.; Lin T. L. "Intense photoluminescence from laterally anodized porous Si", *Appl. Phys. Lett.* **1991**, *59*, 3264-3266.

26. Belomoin, G.; Therrien, J.; Smith, A.; Rao, S.; Twesten, R.; Chaieb, S.; Nayfeh, M. H.; Wagner, L.; Mitas, L. "Observation of a magic discrete family of ultrabright Si nanoparticles", *Appl Phys Lett.* **2002**, *80*, 841-843.

27. Wilson, W.L.; Szajowski, P.F.; Brus, L.E.; "Quantum Confinement in Size-Selected, Surface-Oxidized Silicon Nanocrystals", *Science* **1993**, *262*, 1242-1244.

28. Rogozhina, E.V.; Eckhoff, D.A.; Gratton, E.; Braun, P.V.; "Carboxyl functionalization of ultrasmall luminescent silicon nanoparticles through thermal hydrosilylation", *J. Mater. Chem.* **2006**, *16*, 1421-1430.

Chapter 2: Synthesis of Si nanocrystal

2.1 Introduction

Among various approaches of synthesizing Si nanocrystal, my method of production is rather simpler and mass productive. Electrochemical etching is controlled by defined parameters so that etching results are always reproducible. Etching of one silicon wafer can produce approximately 20 ml of 1 ng/nL Si nanoparticle solution. In this chapter, I describe the experimental procedure of Si nanoparticle synthesis. I also detail parameters of etching and following results of them.

2.2 Synthesis of silicon nanocrystal from silicon wafer

2.2.1 Anodic etching of silicon wafer

Silicon wafer in hydrofluoric acid solution experiences etching of its surface by following reaction.

$$Si+6HF \rightarrow H_2SiF_6 + H_2 + 2H^+ + 2e^- \qquad (2.1)$$

In an electrochemical etching cell (Fig 2.1), silicon wafer is slowly etched with the moving boundary of HF/H_2O/EtOH (1:1:2, v:v:v). Because the etching of wafer is maximized at the air-solution boundary, slow addition of the etching solution is required. Water in an etching solution provides oxidizing of silicon surface for hydrofluoric acid. Water can be substituted with peroxide but the ratio among HF, peroxide and alcohol should strictly be followed because oxidation competes with

etching of wafer's surface. The role of alcohol is to increase the wettability of the wafer surface in an etching solution.

2.2.2 Ultrasonication of silicon wafer

Nanopores on a Si wafer after etching are crumbled into nanoparticles by ultrasonication. Mechanically stripped nanopores' sizes have a broad distribution ranging from 1 nm to a few microns. However, micron-sized chunks are still fluorescence because they have nanoparticles imbedded on their surface. Because my method has an intrinsic problem of a broad size distribution; their size separation is a serious issue. Therefore, after sonication, brownish solution, whose color comes from micron chunks, is filtered to remove at least the particles larger than a few hundreds nanometers.

2.2.3 Experimental section

The overall procedure of synthesis is depicted in Figure 2.2. Silicon wafers (<111> oriented, 0.001~0.01 ohm-cm, Arsenide doped) were purchased from Virginia Semiconductor, Inc., Fredericksburg VA. Wafers were electrochemically etched in a HF: H_2O: Ethanol (2:1:1, volume ratio) mixture using the lateral etching method [1]. Anodic etching was performed in a polycarbonate cell that accommodates a 100 mm dia. Si wafer placed between two Pt wire mesh cathodes. Electric contact was provided to the top edge of the vertically mounted wafer and electrolyte was slowly pumped into cell, hence providing a moving electrolyte boundary. Total etch time typically was about 4 h per 100 mm dia wafer at 120 mA constant current, supplied by a galvanostat (Model 363, EG&G Inc., Princeton, NJ).

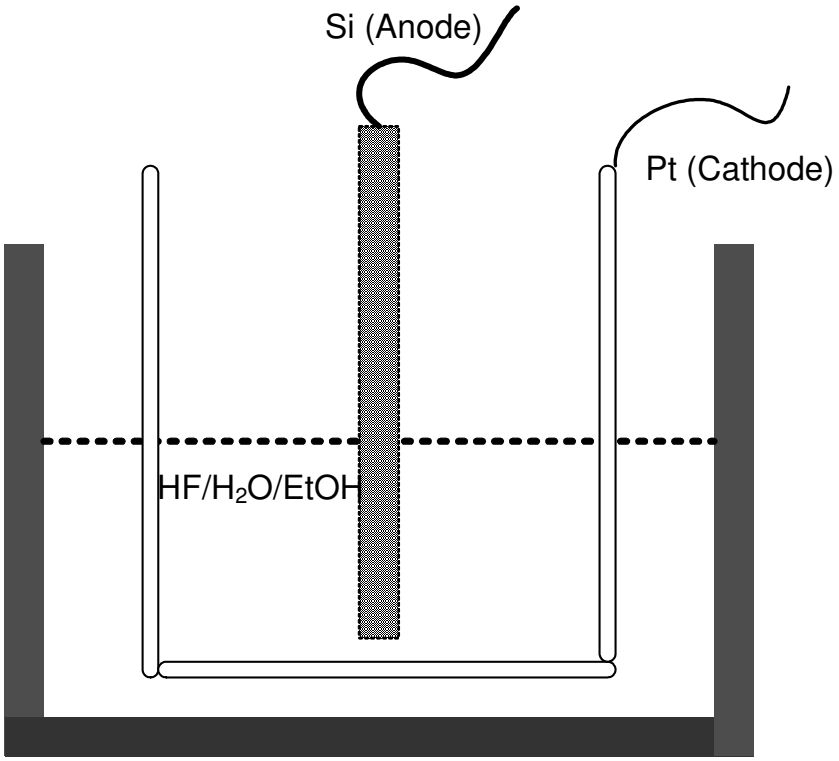

Figure 2.1 Electrochemical anodization bath. Anode: As doped Si wafer, Cathode: Pt Electrolyte: HF+H2O+EtOH, DC current mode: i=5~20 mA/cm2 Moving solution boundary.

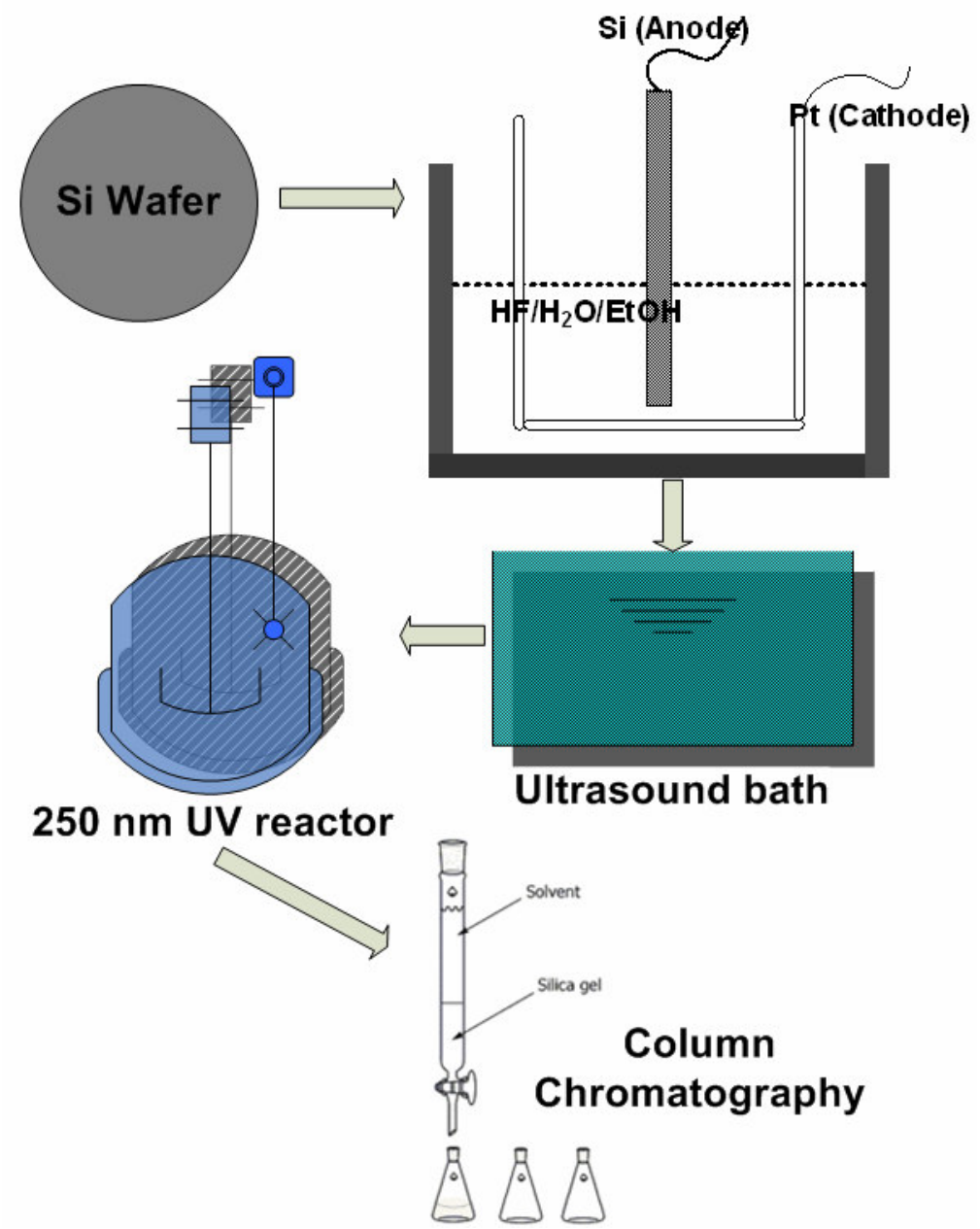

Figure 2.2 Overall process of Si nanocrystal synthesis

Following anodic etching, the wafer is washed with copious amount of deionized water, methanol (HPLC grade, Mallinckrodt Chemicals, Phillipsburg, NJ) and blow-dried with nitrogen gas. Dried wafers displayed an intense orange-red luminescence when excited by a 360 nm UV lamp. Pieces of porous wafer are delivered to measure their morphology by using scanning electron microscopy (Electroscan, OR). Next, Si wafers were sonicated (Ultrasonik, York, PA) in deaerated methanol for two hours under vigorous N_2 purging. Resulting suspension appeared brownish and exhibited weak broadband photoluminescence under UV excitation.

2.3 Results and discussion

2.3.1 Etched Si wafer

Figure 2.3 shows scanning electron microscope image of the porous layer of Si wafer after anodic etching. Images are showing etched pores on a surface of silicon wafer. Pore size and pore density can be tuned with etching parameters. Figure 2.4 compares the various fluorescences from Si wafers etched with different etching parameters. Film on the Si wafer is stripped mechanically by sonicating it in a properly chosen solvent. After mechanically removing the porous film from the wafer with various solvents, I observed that several solvents quenched photoluminescence from the Si nanocrystals. Table 2.1 summarizes several solvents' quenching effect under 360nm UV. Organic solvents like 1-octene and styrene showed red/orange light emission. Ethyl alcohol does not prevent the light emission, and particles shine in orangish color. However, methyl alcohol quenches photoluminescence from the Si nanocrystals although the pale brownish solution is seen under visible light, verifying

the existence of sufficient nanoparticles in the solution. Figure 2.5 shows different fluorescence from Si nanocrystal in solution.

Solvents	Quenching of Si NCs
Ethanol	No
Methanol	Yes
1-Octene	No
Styrene	No
Chloroform	No
Acetonitrile	Yes
Allylamine	No
Acrylic Acid	No

Table 2.1 light emission quenching by solvent

2.3.2 Si nanocrystal solution

Prepared silicon nanocrystal solution has a broad size distribution. Although its fluorescence is orangish or reddish depending on etching parameters, the suspension contained particles of various sizes and emitted across the visible spectrum. Broad distribution of silicon nanocrystal was evident in column and thin layer chromatography which separated different color emitting particles. Figure 2.6 shows the results of color separation from both chromatographic methods. They both show that the synthesized orangish fluorescent sample contained Si nanoparticles of a broad size distribution.

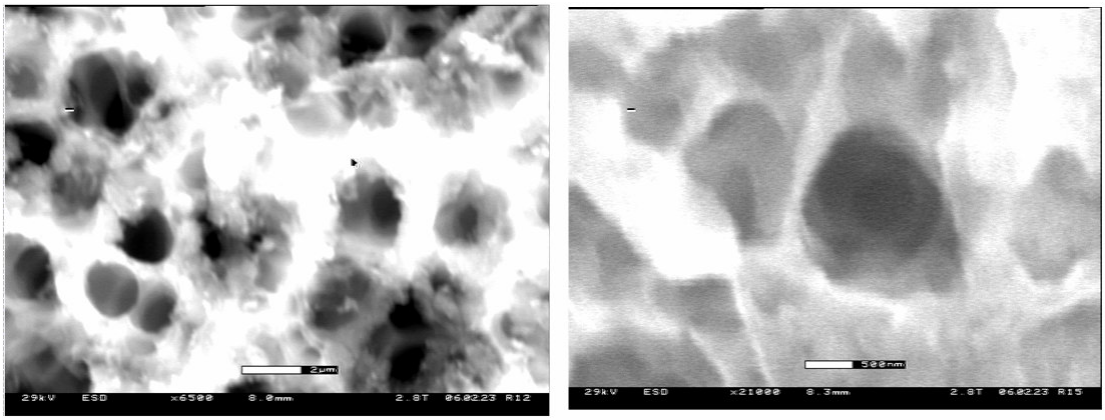

Figure 2.3 SEM image of porous, arsenic (~0.001 ohm·cm) doped Si wafer.

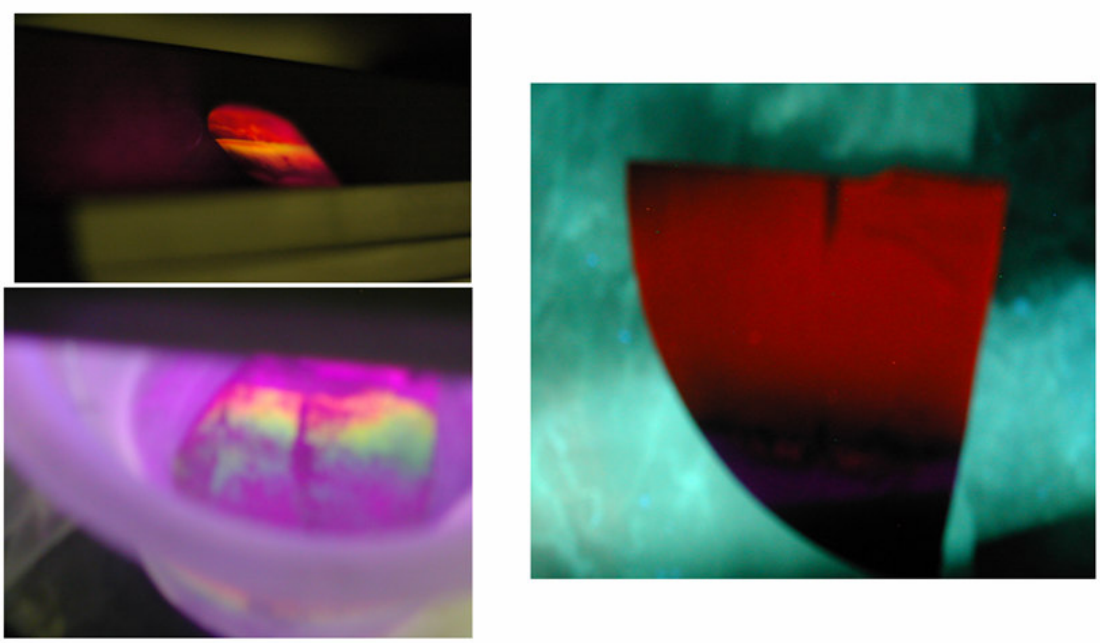

Figure 2.4 Photoluminescence from etched wafers with different etching parameters. All pictures are taken under 360 nm UV lamp excitation.

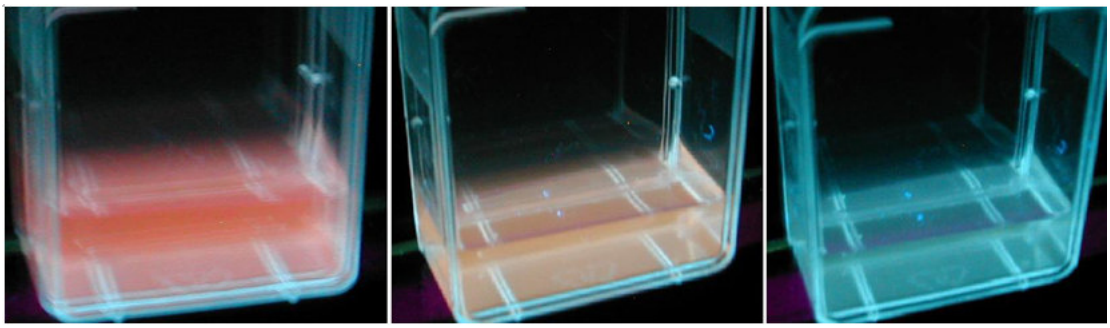

Figure 2.5 Different fluorescence from silicon nanocrystal in a solvent. Fluorescence is observed by UV excitation at 360 nm from the bottom of the each vessel.

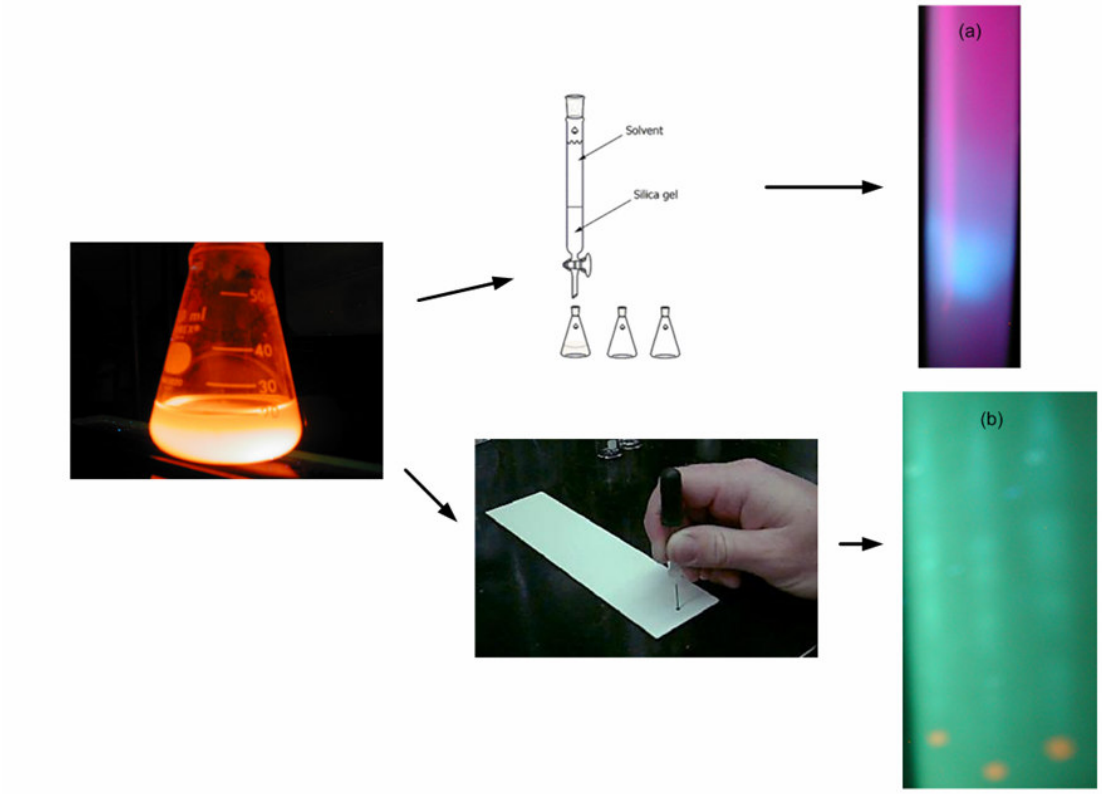

Figure 2.6 Chromatographic separation methods for synthesized bare silicon nanocrystal. (a) Column chromatography with silica gel. (b) Thin layer chromatography.

2.4. Summary

Synthesis of Si nanoparticles by the anodic etching of Si wafer and ultrasonication was successful. Wafer's fluorescence could be tuned by varying etching parameters such as the ratio of acid mixture, current density, or doping material and degree of Si wafer. However, when the nanoporous film on a surface is stripped and crumbled into particles, Si nanoparticle's fluorescence is highly affected by the type of solvent used. Among non-quenching solvents, most of the fluorescence from bare particle solution is red-orange color which means the average sizes of fluorescent particles are around 3.5~4.5 nm in diameter and they have more stable fluorescence than smaller ones.

2.5. References

1. Jung, K. H.; Shih, S.; Hsieh, T. Y.; Kwong, D. L.; Lin T. L. "Intense photoluminescence from laterally anodized porous Si", *Appl. Phys. Lett.* **1991**, *59*, 3264-3266.

Chapter 3: Photo-assisted tuning of Si nanocrystal photoluminescence

3.1 Introduction

Silicon is rather inefficient light emitter due to the indirect-band gap electronic structure, requiring a phonon to balance electron momentum during interband transition. Fortunately, momentum requirements are relaxed in 1-5 nm dia Si crystals as a result of quantum confinement effects and bright photoluminescence in the UV/VIS range is achieved. Photoluminescent Si nanocrystals along with C and SiC based nanoparticles are considered bio-inert and may lead to the development of biocompatible and smaller probes than metal chalcogenide based quantum dots. Published Si nanocrystal production procedures typically do not allow for the fine control of the particle size. An accepted way to make H terminated Si nanocrystals consists of anodic Si wafer etching with subsequent breakup of the porous film in the ultrasound bath. Resulting H-termination provides a useful platform for further chemical derivatization and conjugation to biomolecules. However, a rather polydisperse mixture is produced after the ultrasonic treatment leading to distributed band gap energies and degree of surface passivation. From the technological point of view, a homogeneous nanoparticle size mixture is highly desirable.

In this study, I offer an efficient way to reduce H-terminated Si nanocrystal diameter and narrow size distribution through photo-catalyzed dissolution in the HF/HNO_3 acid mixture. Si particles were produced using lateral etching of Si wafer in

$HF/EtOH/H_20$ bath followed by sonication in a deaerated methanol. Initial suspensions exhibited broad photoluminescence in the red spectral region. Adding an HF/HNO_3 acid mixture to the suspension and exposing it to 340nm light carried out the photo-assisted etching. Photoluminescence and absorbance spectra, measured during the dissolution show gradual particle size decrease as confirmed by the photoluminescence blue shift. Simultaneous narrowing of photoluminescence spectral bandwidth suggests that dissolution rate varies with particle size. I show that Si nanoparticle dissolution follows the shrinking core model that accounts for the etching rate variation with the particle size. Significant improvement in PL quantum yield is observed following acid treatment suggesting improvement in the dangling bond passivation.

3.2. Photo driven size tuning of silicon nanocrystal

3.2.1 UV catalyzed particle etching

Several studies have demonstrated that photo-induced oxidation can produce a PL blue shift in porous Si [1] [2]-[4]. Photo-induced oxidation followed by silicon oxide attack by HF leads to the gradual decrease in the average porous Si surface crystallite size resulting in a blue shift consistent with the band-gap dependence on the nano-particle size [2][5]. In a similar fashion, I expect that wet chemical etching can be applicable to control the size of suspended hydrogen terminated Si nanocrystals. In the current study, I offer an efficient way to reduce the average SN diameter and simultaneously narrow size distribution through photo-catalyzed dissolution. By measuring both absorbance and photoluminescence during particle dissolution, we can track the nanoparticle band-gap growth with shrinking crystal size.

Etching in the HF/HNO_3 acid mixture increases PL quantum yield and homogeneity of particle preparation by improving their surface passivation.

3.2.2 Overall dissolution reaction

It is well known that Si does not dissolve in pure HF and oxidizer is necessary to produce silicon dioxide that reacts vigorously with HF. Overall dissolution reaction can be written in Eq. (3.1) [6].

$$3Si+4HNO_3+18HF \rightarrow 3H_2SiF_6+4NO+8H_2O \qquad (3.1)$$

Swihart et al. has shown that dissolution reaction rate is controlled by the Si surface oxidation rate by nitric acid that is catalyzed under UV illumination [7]. When etched with low concentrations of oxidizer HNO_3, the Si particle surface retains its predominantly H-termination [8]. We show that SN dissolution in the acid mixture follows the shrinking core model and accounts for the dissolution rate dependence on particle size and resulting in a more homogeneous dispersion. Photo-catalyzed acid dissolution may offer a straightforward method to alter SN photoluminescence wavelength and significantly improve SN photoluminescence efficiency. Previously PL profiles have been measured on various size Si nanocrystal preparations (for summary see [9]). A major uncertainty in establishing the PL peak dependence on particle size lies in difficulty of accurately determining particle size in the single nm range. Also, TEM images frequently do not show particle size polydispersity. Photoluminescence excitation measurements on a series of discrete size Si nanoparticles in the range from 1 to 2.9 nm resulted in a power law relation between the band-gap (Eg) and particle diameter (d) [5] $Eg = 3.44/d^{0.5}$, suggesting a significant Eg widening in this size range. Other studies, conducted using Si nanoparticles,

embedded in silicon nitride [10], oxide [11], or encapsulated in the organic shells [12]~[14] all confirmed inverse dependence of the band-gap on Si particle diameter.

3.3. Experimental section

3.3.1 Silicon nanocrystal preparation

Silicon wafers (<111> oriented, 0.001~0.01 ohm-cm, As doped) were purchased from Virginia Semiconductor, Inc., Fredericksburg VA. Wafers were electrochemically etched in a HF: H_2O: Ethanol (2:1:1, volume ratio) mixture using the lateral etching method [15]. Anodic etching was performed in a polycarbonate cell that accommodates a 100 mm dia Si wafer placed between two Pt wire mesh cathodes. Electric contact was provided to the top edge of the vertically mounted wafer and electrolyte was slowly pumped into cell, hence providing a moving electrolyte boundary. Total etch time typically was about 4 h per 100 mm dia wafer at 120 mA constant current, supplied by a galvanostat (Model 363, EG&G Inc., Princeton, NJ). Following anodic etching, wafer is washed with copious amount of deionized water, methanol (HPLC grade, Mallinckrodt Chemicals, Phillipsburg, NJ) and blow-dried with nitrogen gas. Dried wafers displayed an intense orange-red luminescence when excited by a 360 nm UV lamp. Next, Si wafers were sonicated (Ultrasonik, York, PA) in deaerated methanol for two hours under vigorous N_2 purging. Resulting suspension appeared brownish and exhibited weak broadband PL under UV excitation.

3.3.2 Etching of Si nanocrystal with UV

Hydrofluoric acid (48%) and nitric acids (69~70%) both from J.T. Baker, Phillipsburg, PA, were premixed at 10:1 volume ratio and 1 mL of the acid mixture was added to 1 cm fluorimetric quartz cuvette containing 2 mL of Si particle suspension in methanol. Immediately following mixing, the cuvette was exposed to 340 nm light in the photo reactor (RMR-600, Southern New England Ultraviolet Company, Branford, CT). Nitrogen atmosphere was maintained throughout the dissolution process.

3.3.2 Particle characterization

Transmission electron microscope images were acquired using JEOL 2100F Field Emission electron microscope (JEOL Inc., Tokyo, Japan). Samples were prepared by placing a drop of Si nanocrystal suspension in methanol on a carbon grid followed by drying. SN photoluminescence spectra were recorded using spectrofluorimeter (model LM800, SLM Inc.). A quartz cuvette, containing SN suspension and acid mixture was removed briefly from the photo-reactor at various reaction stages and PL spectra at 360 nm excitation were recorded. Absorbance spectra during Si suspension dissolution were recorded after adding 10 μl of the 10:1 HF/HNO_3 mixture with Ocean Optics (Dunedin, FL) Chem2000 fiber optic spectrophotometer. Time resolved PL measurements were carried out on Photon Technology International (Lawrencville, NJ) spectrometer equipped with GL-3300 nitrogen laser. SN particle size distribution was analyzed with dynamic light scattering based sub-micron particle analyzer (Model N4MD, Coulter, Inc.).

3.4. Results and discussion

3.4.1 TEM

TEM images of particles, acquired on a carbon grid by depositing and evaporating a drop of Si particle suspension in methanol confirm the presence of a polydisperse mixture of nanometer size crystals (Fig. 3.1) and a lattice spacing, characteristic for the (111) planes in the diamond-like Si lattice is visible in the high resolution image of an 8 nm dia particle (right panel of Fig. 3.1)

3.4.2 In-situ absorption spectra

Initial absorbance spectrum of the Si NP suspension in methanol (upper curve on Fig. 3.2.), recorded prior to the acid mixture addition can be deconvoluted into the sum of $1/\lambda^n$ scattering component and two Gaussian oscillators centered at 249 and 311 nm. A significant scattering component in the Si NP absorbance is caused by a sub-population of micron-sized particles, as indicated by dynamic light scattering measurement (Fig. 3.3). The strongest absorbance features in the bulk Si were assigned to the direct inter-band transitions at the Γ point of the Brillouin zone [9], however, they are blue shifted 0.8 eV and 0.6 eV respectively in our Si crystals as a result of quantum confinement in nanometer diameter crystals [16]. Absorbance increase with photon energy below 400 nm is typical for the spectra of bulk Si reflecting the slow onset of the indirect transition $\Gamma \rightarrow X$ [9].

Introduction of the 10 μl 1:10 $HF:HNO_3$ acid mixture to Si particle suspension together with exposure to the 340 nm light results in exponential absorbance drop (Fig. 3.2. insert) and spectral shape evolution consistent with the average particle size

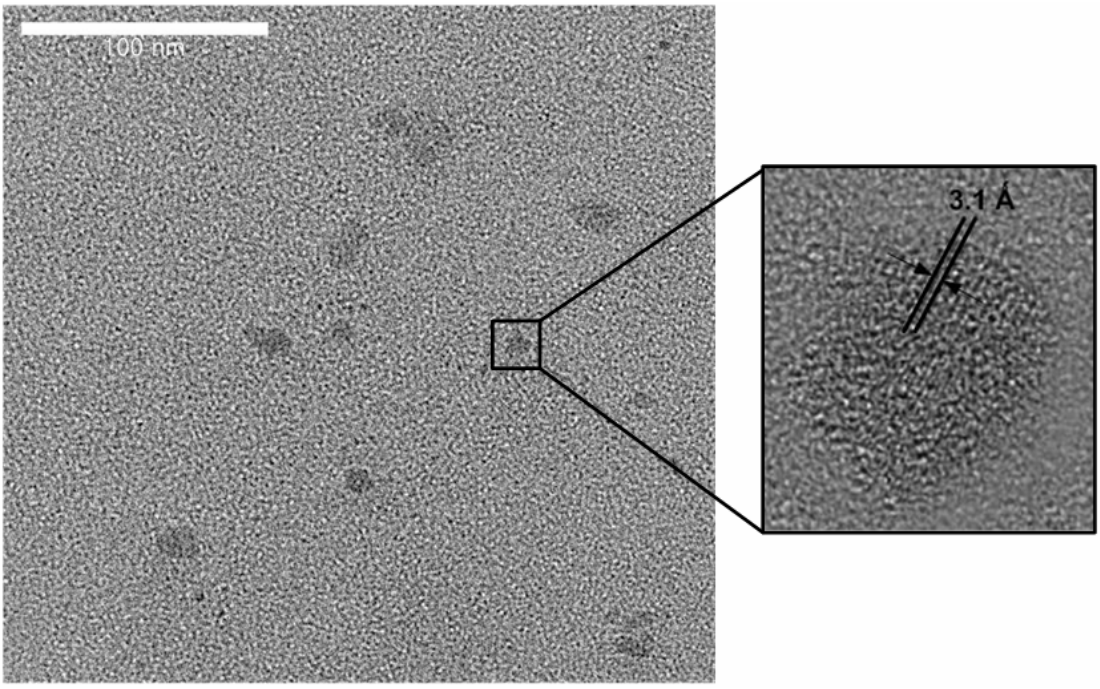

Figure 3.1 TEM images of the Si nanocrystals prior to dissolution. Right panel shows a high-resolution image of an 8 nm dia particle with visible lattice planes.

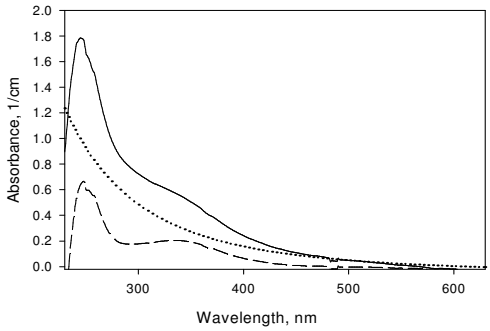

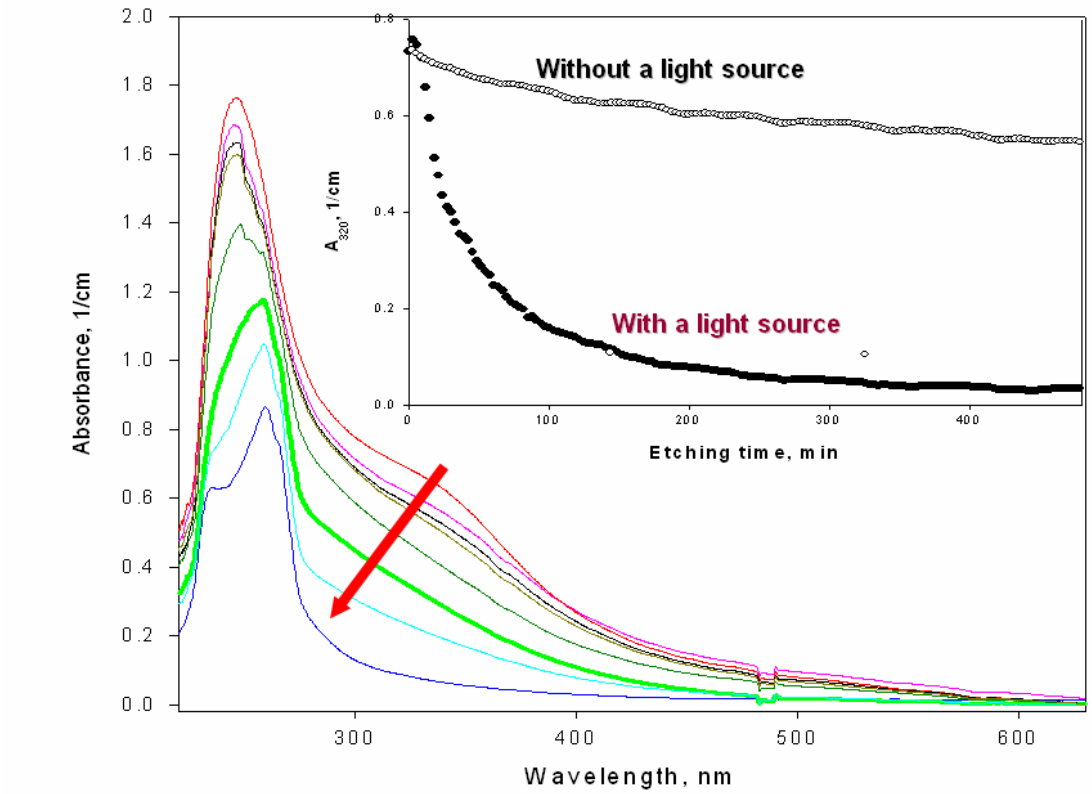

Figure 3.2 Si particle suspensions in methanol. (Top) Absorbance of freshly prepared particles (solid line) decomposed into scattering (dotted line) and absorbing (dashed line) components. (Bottom) Absorbance evolution after the introduction of the 10 micro liters of 10:1 HF/HNO_3 mixture and exposure to UV light. Insert compares the 320 nm absorbance decay rates with and without UV exposure (full and open circles respectively). T=293K.

reduction. The dissolution reaction is noticeably photo-catalyzed as the dissolution rate (estimated from the time required to achieve equivalent absorbance change, increases about 20 times upon exposure to UV light (see Fig. 3.2 insert). A pronounced reduction of the scattering component is observed in the initial dissolution stage (t<30 min), indicating the removal of larger particles. Particle size distribution acquired from the dynamic light scattering measurement supports the significant reduction of the average particle size with the median diameter in the 5 nm range (Fig. 3.3). Visually the suspension turns totally transparent in about 15 min. Gaussian component amplitudes at 311 nm and 249 nm gradually decrease during the course of dissolution with both peaks experiencing wavelength shifts. The lower energy feature blue shifts from 311 nm (3.9 eV) prior to acid addition to about 290 nm (4.3 eV) after 2 h photo-catalyzed dissolution, while the 249 nm (4.97 eV) band red shifts to 258 nm (4.81 eV) (Fig. 3.2). An intermittent fine structure was also observed in the 250 nm absorbance peak. It is notable that absorbance reaches a limiting value in about 5 h indicating the remarkable stability of the smallest crystals against further dissolution even after the introduction of additional acid mixture. Koshida has described the effect of dissolution photo tuning when nano-porous Si wafer was etched in HF [2][3]. Following their interpretation, Si dissolution in HF is significantly retarded in the absence of the UV light induced oxidation. As the particle size shrinks, the band-gap expands (as established in our investigation by the absorbance edge shift in Fig. 3.2.) and ultimately can exceed the energy of the UV lamp photons ($h\nu \sim 3.7$ eV) thus hindering further light-induced oxidation.

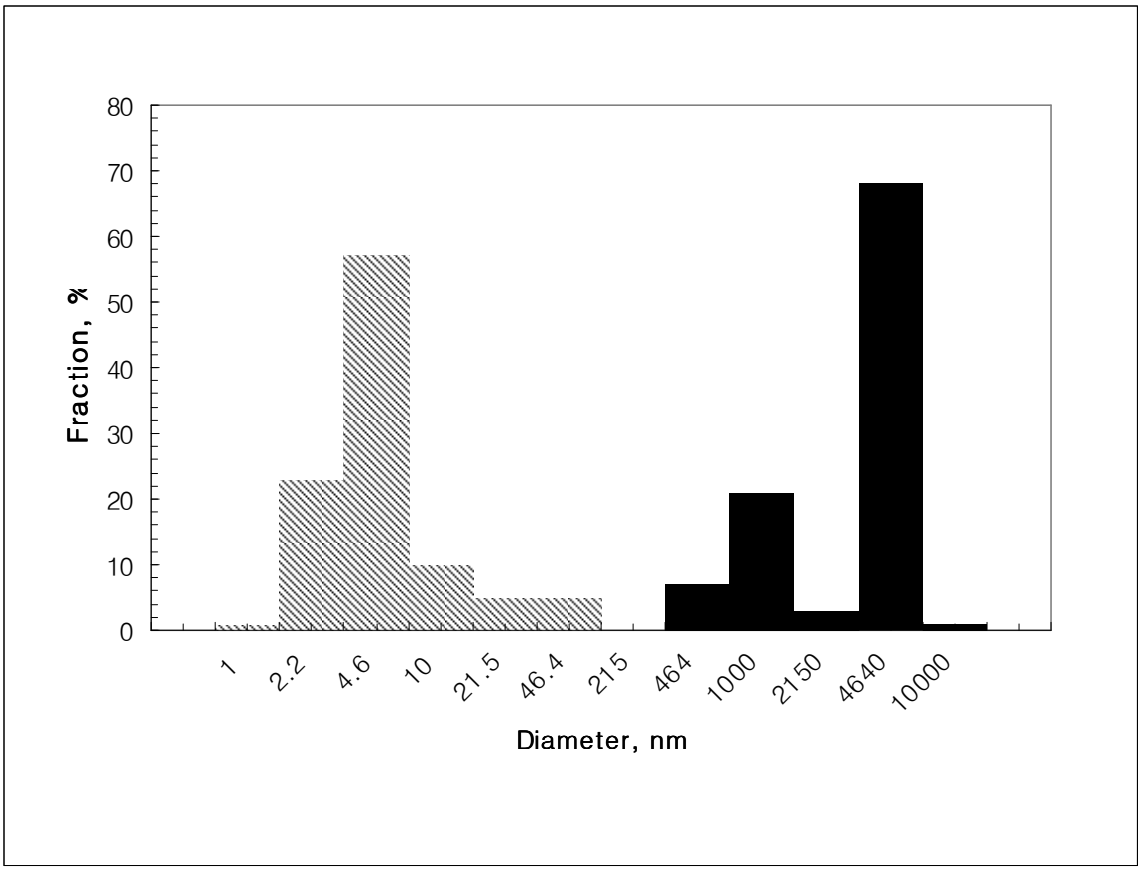

Figure 3.3 Si particle size distribution, estimated using from dynamic light scattering measurement. Full bars represent suspension following Si wafer sonication in methanol, shaded bars- after 30 min photo-catalyzed etch in HF/HNO_3 mixture.

Another possible reason for the Si dissolution self-limitation could be the inverse oxidation rate dependence with particle size, as reported by Okada et al. [17]. However, their study was performed with larger Si particles (20<d<500 nm) and is not obvious whether this dependence can be extrapolated to smaller Si crystals in the single nanometer range. A specially designed study would be required to evaluate the possible role of these mechanisms in hampering the complete Si nanoparticle dissolution.

3.4.3 In-situ fluorescence spectra

PL of Si nanoparticles during the photo-catalyzed dissolution blue shifts across the wide range of the visible spectrum is consistent with the gradual average size particle reduction. Extent of the PL shift was limited to the blue-green region in most experiments prior to intensity drop below the detector sensitivity limit. However, several samples demonstrated PL shifts up to 400 nm. The dissolution reaction is visibly photo-driven as evidenced by the stratified multicolor PL pattern in a sample cell that was illuminated through the bottom cell wall with a 340nm lamp (Fig. 3.4). Consistent with the Si particle suspension absorbance spectrum (see upper trace in Fig. 3.2) the 340 nm light from the UV lamp would be gradually attenuated along the vertical dimension, and, consequently, will result in slower dissolution. Given that PL colors can be directly related to a discrete series of Si particle sizes in the range from 1.67 nm to 3.7 nm [5], the stratified PL pattern reflects the distribution of particles sizes as a result of varying dissolution rate along the cuvette height (Fig. 3.5.).

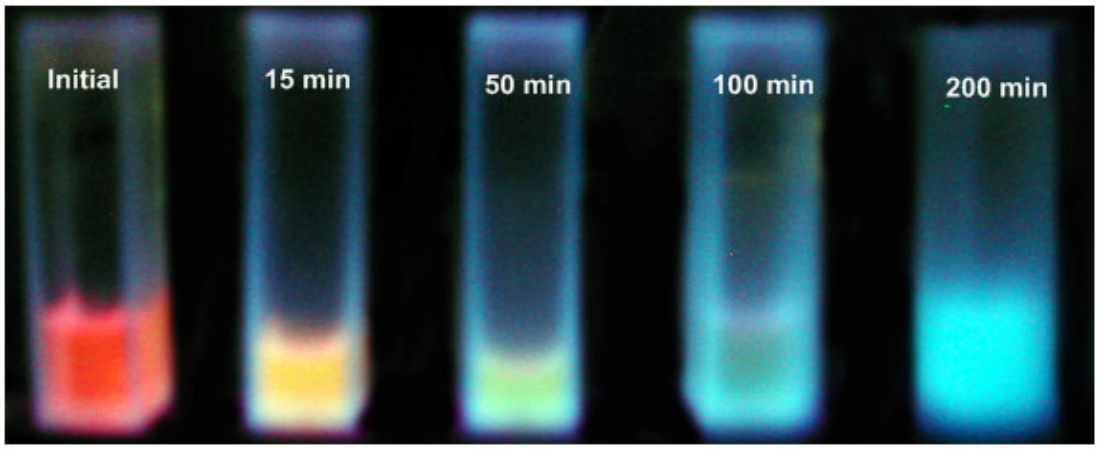

Figure 3.4 Si particle photoluminescence recorded during various stages of photo-catalyzed dissolution in the acid mixture. $\lambda_{exc} = 360$ nm.

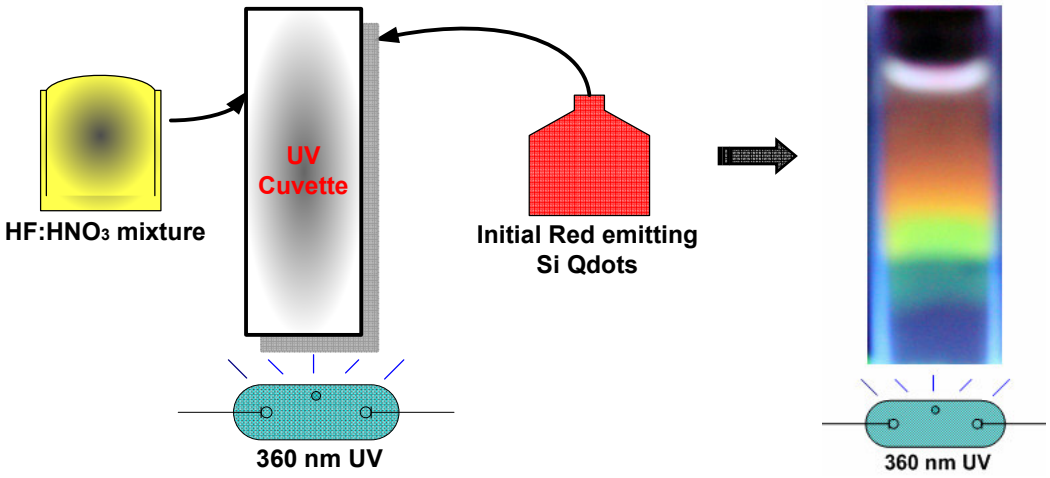

Figure 3.5 Multicolor photoluminescence pattern in the stationary Si nanoparticle suspension during the UV catalyzed acid dissolution. Sample cell was illuminated at 340 nm through the bottom cell window.

3.4.4 Photoluminescence variation with the dissolution of Si nanocrystal

Si particle PL (λ_{exc}=360nm) was measured during the dissolution process using scanning spectrofluorimeter (Fig. 3.6). Spectra were recorded by moving Si particle and acid containing quartz cuvette from the UV reactor to the fluorimeter sample compartment for the duration of the scan (~30sec). Typically, the PL spectrum prior to acid introduction contains a broad emission peaking at 650 nm (Fig. 3.6). Adding the acid mixture and exposing suspension to 340 nm light result in a smooth blue shift of the broad PL feature as shown in Fig. 3.6. PL peak intensity and bandwidth also noticeably varied throughout the course of particle dissolution. PL peak intensity rises with the commencement of the reaction, reaches a maximum value at λ=560 nm, and gradually declines with further wavelength shift to the green-blue region. The final peak PL wavelength typically is in the interval 460-510 nm before emission becomes undetectable. If decreasing particle size were the only factor responsible for the PL blue-shift due to quantum confinement, we would expect a further emission wavelength shift as suggested by higher band gap values consistent with the absorbance spectra (Fig. 3.2). In a study of oxidized nanoporous Si, Wolkin et al. has shown that exciton recombination proceeds through the defect levels in the band gap if Si surface is exposed to oxygen [18]. PL experiments, conducted in strict anaerobic conditions led to the conclusion that the presence of Si=O bond introduces electron and hole trap levels in Si nanocrystal band-gap thus effectively limiting the emission energy to about 2.1 eV even in the smallest particles. In a theoretical study, Zhou et al. have determined that band gap can be lowered by 1.5eV –2.4eV in 1nm and1.4nm Si nanocrystals when H passivation is replaced with hydroxyl [19].

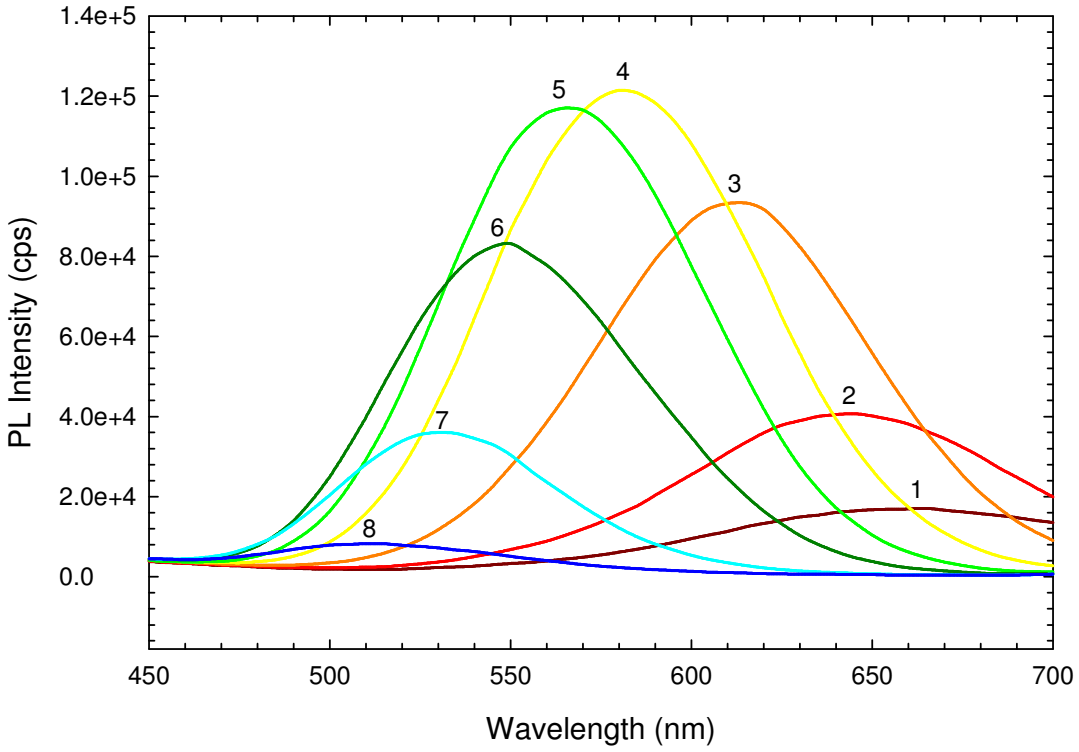

Figure 3.6 Photoluminescence spectra recorded during photo-catalyzed Si nanoparticle dissolution: 1) prior to acid introduction, 2) 30min after acid addition, 3) 50min, 4) 80min, 5) 110min, 6) 130min, 7) 170min, 8) 200min.

As our experiments were conducted in the deoxygenated solutions that contained HF, the extensive Si surface oxidation is suppressed. However, exposure to HNO_3 and UV light may facilitate the partial passivation by oxygen that competes with Si-H bond, a prevalent surface functionality in the HF environment [20]. The sensitivity of the final PL wavelength to the presence of residual oxygen thus illustrates a competition between H and the various oxygen species in the Si particle passivating shell.

3.4.5 Direct interband transition

PL decay lifetime data shows the different nature of optical transitions occurring in the blue and yellow-green particle populations. We have measured the average PL decay lifetime to be t=6 ns when a blue particle subpopulation (λ_{exc} =420nm; λ_{exc} = 360nm) was selectively excited. Such values are consistent with the dipole allowed direct inter-band transitions that are expected for H-terminated nanocrystals [19]. In contrast, during Si particle suspension etching induced PL shift from red to green, the measured radiative lifetimes were in the range from $5x10^{-5}$ to 10^{-5}s, typical for the indirect transitions. It was suggested previously that oxide passivation creates a dipole-forbidden "indirect gap" that may be up to 2.3 eV smaller than the direct gap in the 1nm dia H-passivated species [19].

3.4.6 Narrowing of size distribution

It is notable that PL peak bandwidth is gradually reduced all the way through the photo-catalyzed reaction (Fig. 3.6.) Full width at half maximum (FWHM) of the initial red PL band decreases from 1.1± 0.1 eV to 0.4±0.15 eV for particles with blue-green PL (Fig. 3.6). Given that at a single Si nanoparticle level FWHM is about 0.2

eV [13], it indicates a considerable narrowing of the emissive particle size dispersion during the dissolution process. Narrowing of particle size polydispersity is also supported by the absorbance spectra evolution (Fig. 3.2.), however a direct comparison with PL can hardly be made as different particle subpopulations are represented in these two measurements. While Si particles of all sizes contribute to the absorbance signal, only the emissive or "bright" nanocrystals are represented in PL. The fraction of "bright" particles controls the overall PL efficiency since this parameter can exceed 90% at a single Si nanocrystal level [21]. External quantum yield, measured relative to quinine sulfate standard in our Si suspensions was up to 60% in samples exhibiting yellow PL. Taken together with the microsecond PL decay rates, high QY values point to a sluggish nonradiative recombination even in the oxide passivated Si nanocrystals and a relatively defect-free particle structure. The dissolution reaction can be stopped and PL stabilized at any stage by either turning off the UV light or diluting the suspension with methanol.

3.5. Particle dissolution modeling

3.5.1 Photo driven Si dissolution

It has been studied that photo induced oxidation produces a blue shift in PL from porous wafers [22]~[25]. I expected similar phenomena in Si nanocrystals when there is UV light illumination during dissolution reaction. Dissolution of the Si particles in HF and HNO_3 mixture competes with oxidation of Si-H by nitric acid and etching of the oxide by hydrofluoric acid [8]. In our experiment, I observed that UV light strongly catalyzes the oxidation part of this competing reaction. Table 3.1 summarizes the UV effect on the dissolution reaction.

Parameters	Reaction rate	Comments
Amount of etching solution per sample	Increase	Dissolution rate is linearly dependent on the amount of added acids mixture
Acid composition of etching solution	Increase with the amount of oxidizing agent	Rate increases with the input of oxidizer
Ambient air	Increase	Ambient air provide the oxygen
UV light	Increase	Dramatically increase the reaction rate

Table 3.1 Important parameters involved in the dissolution reaction

Dissolution reaction rate is primarily dependent on the UV light source comparing with other parameters like amount of acids, ratio of acid mixture and temperature, etc. We measured the dissolution rate with the strength of the UV light source by varying the number of light bulbs in the UV reactor. I assume light intensity is directly related to the number of lamps. Table 3.2 summarizes the effect of UV light strength.

Number of UV lamps	Reaction time (min)
0	200
1	8
8	2

Table 3.2 Effect of UV strength on the reaction rate with fixed acid concentration.

3.5.2 Modeling of Si nanocrystal dissolution

I have modeled Si particle dissolution using a shrinking core approximation that is frequently utilized in small particle dissolution simulations [26]. Our

calculation is limited only to the emissive or photoluminescent fraction of the Si particle suspension and does not account for larger or "dark" particles. Initial "bright" particle size distribution curve can be approximated with a lognormal distribution assuming that the experimental PL profile reflects size polydispersity with a single particle PL FWHM=0.2 eV [13]. Therefore, we can fit the initial PL curve to the lognormal distribution using the relationship between particle size and PL wavelength. Equation (3.2) represents the lognormal distribution of the sample.

$$\frac{F(d,0)}{N_0} = \frac{\exp\left[-\frac{\left(\ln\frac{d}{d_g}\right)^2}{2\left(\ln\sigma_2\right)^2}\right]}{d\ln\sigma_2\sqrt{2\pi}} \tag{3.2}$$

where F(d,0) is initial fraction of particles with diameter d, N_0 is total particle number, and d_g and σ_2 are determined from the experimental distribution. Figure 6 compares the curves generated from the lognormal distribution and the experimental PL profile. Using the relationships between the particle's diameter and the PL emission wavelength we can relate the 650 nm PL peak with the largest fraction of Si particles with d=5 nm. The lognormal distribution also includes larger particles (>5 nm), which initially do not contribute to visible PL. I assume that the reaction rate is controlled by the mass transport of the acid mixture to the Si NP surface. At steady state, the acid reaction rate at the surface of the nanoparticle is assumed to be equal to the rate of external acid diffusion to the nanoparticle surface.

$$-r_{Acid\_surface} = k_r C_{Acid\_surface} = k_c\left[C_{Acid\,0} - C_{Acid\_surface}\right] \tag{3.3}$$

Solving Equation (3.3) for $C_{Acid\_surface}$ gives,

$$-r_{Acid} = k_r C_{Acid\_surface} = \frac{k_r k_c}{k_r + k_c} C_{Acid0} \tag{3.4}$$

where C_{Acid} - acid concentration, r_{Acid} - acid consumption rate, k_r -dissolution reaction rate constant and k_c - mass transfer coefficient of the acid mixture [26].

Mass transfer coefficient is obtained from the Frossling correlation:

$$Sh = \frac{k_c d}{D_{Acid\_SiNP}} = 2.0 + 0.6\,\mathrm{Re}^{1/2}\, Sc^{1/3} \tag{3.5}$$

where Sh – Sherwood number, D_{Acid_SiNP} - component diffusion coefficient, Re - Reynolds number, and Sc - Schmidt number. For small particles, Sh ≈ 2, and mass transfer constant can be simplified as:

$$Sh = 2.0 + 0.6\left(\frac{\upsilon_s d}{\nu}\right)^{1/2}\left(\frac{\nu}{D}\right)^{1/3} = \frac{k_c d}{D_{Acid\_SiNP}} = 2.0\ \left(d\ is\ very\ small\right) \tag{3.6}$$

Where υ_s is the mean fluid velocity, ν is the kinematic fluid viscosity, D - mass diffusivity. The reaction rate can be expressed by combining Eq. (3.6) and Eq. (3.4):

$$-r_{Acid} = \frac{k_r k_c}{k_r + k_c} C_{Acid0} = \frac{k_r C_{Acid0}}{1 + \frac{k_r}{k_c}} = \frac{k_r C_{Acid0}}{1 + \frac{k_r d}{2D_{Acid\_SiNP}}} = \frac{k_r C_{Acid0}}{1 + \frac{d}{d^*}} \tag{3.7}$$

where $d^* = \frac{2D_{Acid\_SiNP}}{k_r}$.

Since 6 moles of acid react with 1 mole of Si (see Reaction (3.1)), $-\frac{1}{6} r_{Acid} = -r_{SiNP}$, the relationship between the particle diameter-d and reaction time-t can be derived using mass balance equation (3.8):

$$0(in) - 0(out) + r_{SiNP}\pi d^2\left(generation\right) = \frac{d[\rho_{SiNP} V]}{dt}\left(accumulation\right) \tag{3.8}$$

$$\frac{\mathrm{d}\,d}{\mathrm{d}\,t}=\frac{r_{SiNP}}{\rho_{SiNP}}=-\frac{\left(-r_{Acid}\right)}{3\rho_{SiNP}}=\frac{-1}{3\rho_{SiNP}}\left[\frac{k_r C_{Acid}}{1+\dfrac{d}{d^*}}\right]=-\frac{\alpha}{1+d/d^*} \tag{3.9}$$

where $\alpha=\dfrac{k_r C_{Acid\,0}}{3\rho_{SiNP}}$, and ρ_{SiNC} - Si NP density.

In order to account for the polydisperse sample nature, we choose the narrow interval d from the particle size distribution function (Figure 3.7) and derive the balance equation for that interval [26]:

$$R(d)\,F(d,t)\big|_{d}-R(d)\,F(d,t)\big|_{d+\triangle d}=\frac{\partial\left[F(d,t)\triangle d\right]}{\partial t} \tag{3.10}$$

where $R(d)=\dfrac{\mathrm{d}\,d}{\mathrm{d}\,t}=-\dfrac{\alpha}{1+d/d^*}$ is the growth rate of particles of diameter d (nm/sec).

Equation (3.10) is simplified as [26],

$$\frac{\partial F(d,t)}{\partial t}+R(d)\frac{\partial F(d,t)}{\partial d}+F(d,t)\frac{\partial R(d)}{\partial d}=0 \tag{3.11}$$

Solving the ordinary differential equation of $F(d,t)$ in terms of the reaction time t by substituting $R(d)=-\dfrac{\alpha}{1+d/d^*}$ we obtain the distribution curve at the specific reaction time, t (Equation 3.9).

$$F(d,t)=\frac{N_0}{d^*}\frac{\left(1+d/d^*\right)}{\ln\sigma_2\sqrt{2\pi}}\sqrt{\left(1+d\Big/d^*+\frac{2\alpha t}{d^*}\right)^{-2}}\left(\sqrt{\left(1+d/d^*\right)^2+\frac{2\alpha t}{d^*}}-1\right)^{-1}\frac{1}{2\ln\sigma_2}\exp\left(-\ln\frac{\sqrt{\left(1+d/d^*\right)^2+\dfrac{2\alpha t}{d^*}}-1}{d_r}\right)^2 \tag{3.12}$$

where N_0 - total initial particle number and parameters σ_2, $d_r=d_g\big/d^*$ can be estimated from the initial particle size distribution, Eq. (3.2).

3.5.3 Modeling results and discussion

I have calculated a series of Si particle size distribution profiles according to Eq. 3.12 (Fig. 3.8) using Mathematica (ver 5.2, Wolfram Research, Champaign, IL) software package. Profile genesis can be compared with the PL spectra, acquired during our Si particle suspension dissolution, (Fig. 3.6) given that PL peak wavelength tracks Si particle size. Consequently, PL intensity profile would result from the additive effect of certain size particles, and can be directly related to their density within a fixed size interval.

The major characteristics of the PL profile change during the dissolution are simulated by our calculation. First, the median particle size is monotonically reduced leading to the blue PL shift. Using the size-band gap relation for H-terminated spherical Si nanocrystals given in [5] we can deduce from our PL peak position (Fig. 3.6) that the median particle diameter is reduced from 3.2 to 1.5 nm in the course of 2 h dissolution. Further particle size reduction may not be reflected by PL wavelength shift due to oxidation induced band gap narrowing, as suggested by Wolkin et al. [18].

Second, an accumulation of particles with median diameter d=2.2 nm is predicted by dissolution simulation peak of curve #3 in Fig. 3.8. PL intensity in our dissolution experiments always peaked in the green-yellow range around λ_{em}=520-540 nm (2.4 eV), and is consistent with the emission from 2 nm dia H-terminated Si particles [5].

A third notable characteristic, predicted by our simulation, is monotonic reduction of particle size polydispersity during dissolution reaction.

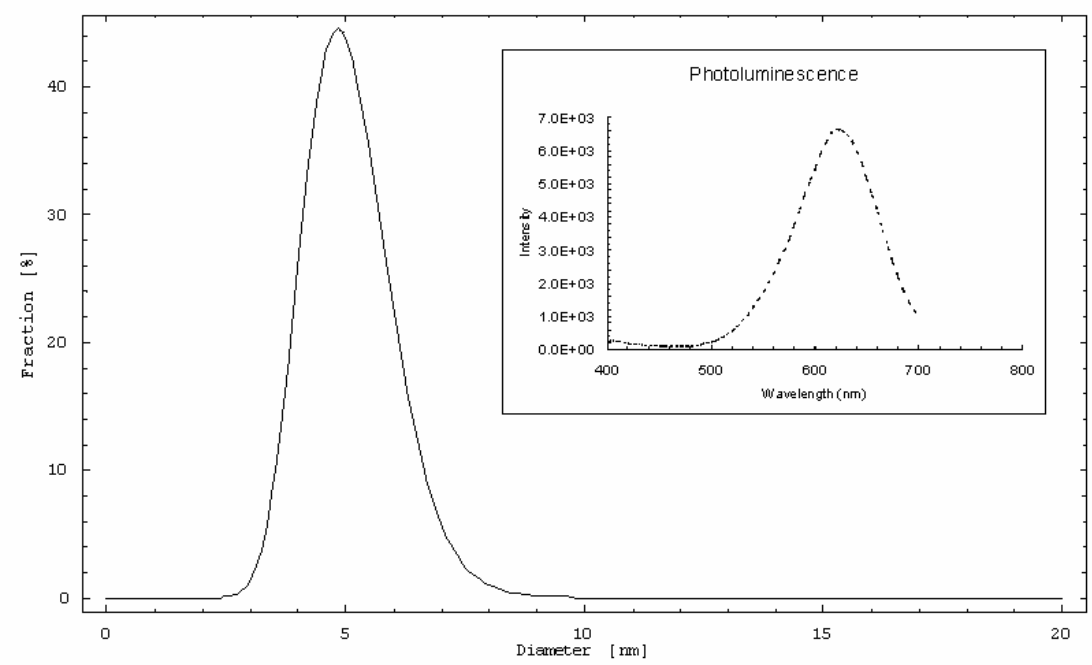

Figure 3.7 Initial Si nanocrystal size distribution function used in the dissolution model. Inset shows the suspension photoluminescence profile. λ_{exc} = 360nm.

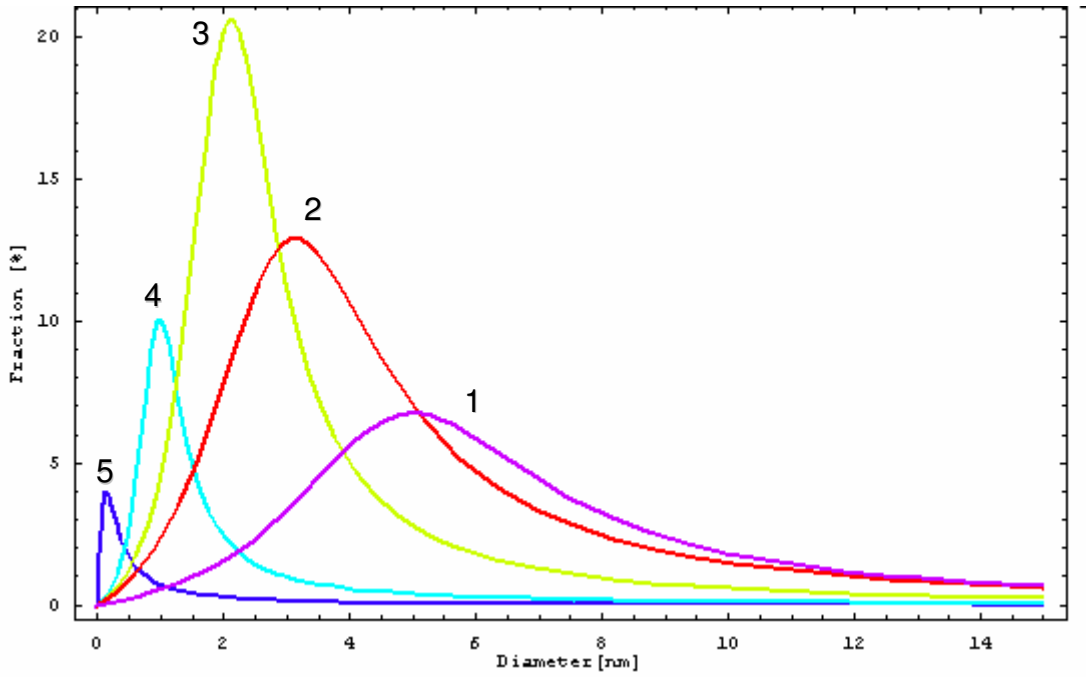

Figure 3.8 Simulated distribution functions during Si nanoparticle suspension dissolution in acid mixture. Equation (12) input parameters $N_0 = 10^4$, d* = 5, $\alpha = 0.2$, $\sigma_2 = 1.5$ and $d_r = 5$. 1) Initial distribution, 2) 17min after acid addition, 3) 50 min, 4) 100 min, 5) 200 min.

Initially, we obtained a rather broad nanometer size population along with the micron size particles after wafer etching and sonication (Fig. 3.3), therefore a reduction in polydispersity would be highly desirable for practical nanocrystal applications. Indeed, a significant reduction of PL peak width (Fig. 3.9) and absorbance edge slope (Fig. 3.2) both reflect a progressively homogeneous mixture.

3.6. Summary

In summary, hydrogen terminated Si nanoparticle photoluminescence wavelength and intensity can be tuned using photo-induced dissolution in HF/HNO3 acid mixture. By measuring both absorbance and photoluminescence during particle dissolution, we have tracked the Si nanoparticle band-gap growth with shrinking crystal size. Etching of Si nanoparticle methanol suspension in the HF/HNO_3 acid mixture increases PL QY up to 60%. Microsecond PL decay rates are consistent with indirect radiative recombination mechanism in particles exhibiting red to green PL. Together with high quantum yield it implies a slow nonradiative recombination and reflect a relatively defect-free particle structure. Nanosecond decay times were recorded in Si particles with blue PL thus suggesting a direct interband transition and, possibly, a different emission mechanism. Our simple etching procedure can be employed to control particle size and prepare bright Si nanoparticle suspensions with emissions spanning the visible range, required for biological fluorescence tagging. A considerable narrowing of particle size distribution was observed during dissolution as predicted by the dissolution reaction simulation using a shrinking core model.

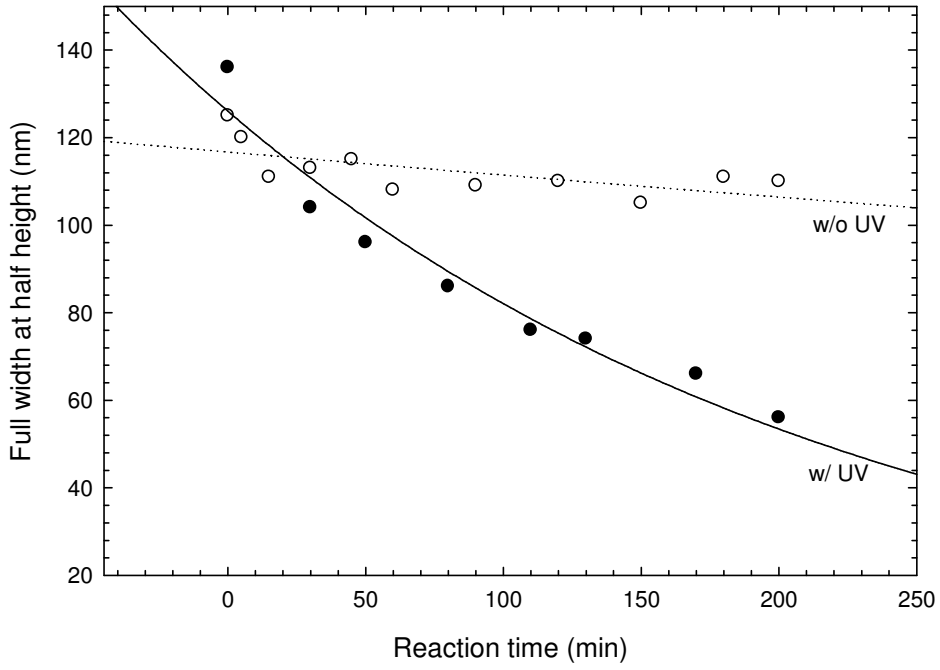

Figure 3.9 Photoluminescence bandwidth at half maximum during the photo-catalyzed dissolution reaction of Si nanocrystal suspension in HF/HNO_3 mixture. Black dots with solid trend line is a FWHH with UV supported experiment. White dots with dotted trend line is a FWHH changes without UV support.

Reaction rate dependence on particle size, predicted by our modeling was in reasonable agreement with our experimental findings. Absorbance and PL results both suggest that the median particle diameter is reduced from 5 nm to less than 1 nm, however, the smallest particles resist complete dissolution even at elevated acid concentrations. Further studies would be focused on clarifying this phenomenon and establishing optical properties with the direct size measurement of Si crystals in the sub-nanometer range.

3.7. References

1. Yamani, Z.; Ashhab, S.; Nayfeh, A.; Thompson, W. H.; Nayfeh, M. "Red to green rainbow photoluminescence from unoxidized silicon nanocrystallites", *J. Appl. Phys.* **1998**, *83*, 3929-3931.
2. Koyama, H.; Koshida, N. "Photo-assisted tuning of luminescence from porous silicon", *J. Appl. Phys.* **1993**, *74*, 6365-6367.
3. Mizuno, H.; Koyama, H.; Koshida, N. "Oxide-free blue photoluminescence from photochemically etched porous silicon", *Appl. Phys. Lett*. **1996**, *69*, 3779-3781.
4. Seraphin, A. A.; Werwa, E.; Kolenbrander, K. D. "Influence of nanostructure size on the luminescence behavior of silicon nanoparticle thin films", *J. Mater. Res.,* **1997**, *12*, 3386-3392.
5. Belomoin, G.; Therrien, J.; Smith, A.; Rao, S.; Twesten, R.; Chaieb, S.; Nayfeh, M. H.; Wagner, L.; Mitas, L. "Observation of a magic discrete family of ultrabright Si nanoparticles", *Appl Phys Lett.* **2002**, *80*, 841-843.

6. Steinert, M.; Acker, J.; Henßge, A.; Wetzig, K. "Experimental Studies on the Mechanism of Wet Chemical Etching of Silicon in HF/HNO_3 Mixtures", *J. Electrochem. Soc*. **2005**, *152*, C843-C850.
7. Li, X.; He, Y.; Talukdar, S. S.; Swihart, M. T. "Process for Preparing Macroscopic Quantities of Brightly Photoluminescent Silicon Nanoparticles with Emission Spanning the Visible Spectrum", *Langmuir*, **2003**, *19*, 8490-8496.
8. Hua, F.; Swihart, M. T.; Ruckenstein, E. "Efficient Surface Grafting of Luminescent Silicon Quantum Dots by Photoinitiated Hydrosilylation", *Langmuir* **2005**, *21*, 6054-6062.
9. Wilcoxon, J.P.; Samara, G.A.; Provencio, P.N.; "Optical and electronic properties of Si nanoclusters synthesized in inverse micelles", *Phys. Rev. B.* **1999**, *60*, 2704-2714.
10. Kim, T.W.; Cho, C.H.; Kim, B. H.; Park, S. J.; "Quantum confinement effect in crystalline silicon quantum dots in silicon nitride grown using SiH_4 and NH_3", *Appl. Phys. Lett.* **2006**, *88*, 123102-123103.
11. Kanemitsu, Y.; "Luminescence properties of nanometer-sized Si crystallites: Core and surface states", *Phys. Rev. B.* **1994**, *49*, 16845-16848.
12. Rogozhina, E.V.; Eckhoff, D.A.; Gratton, E.; Braun, P.V.; "Carboxyl functionalization of ultrasmall luminescent silicon nanoparticles through thermal hydrosilylation", *J. Mater. Chem.* **2006**, *16*, 1421-1430.
13. English, D. S.; Pell, L. E.; Yu, Z.; Barbara, P. F.; Korgel, B. A. "Size Tunable Visible Luminescence from Individual Organic Monolayer Stabilized Silicon Nanocrystal Quantum Dots" *Nanoletters* **2002**, *2*, 681-685.

14. Warner, J.H.; Hoshino, A.; Yamamoto, K.; Tilley, R.D.; "Water-Soluble Photoluminescent Silicon Quantum Dots", *Angew. Chem. Int. Ed.* **2005**, *44*, 4550-4554.

15. Jung, K. H.; Shih, S.; Hsieh, T. Y.; Kwong, D. L.; Lin T. L. "Intense photoluminescence from laterally anodized porous Si", *Appl. Phys. Lett.* **1991**, *59*, 3264-3266.

16. Brus, L.E.; Szajowski, P.F.; Wilson, W.L.; Harris, T.D.; Schuppler, S.; Citrin, P.H.; "Electronic Spectroscopy and Photophysics of Si Nanocrystals: Relationship to Bulk c-Si and Porous Si", *J. Am. Chem. Soc.* **1995**, *117*, 2915-2922.

17. Okada, R.; Iijima, S.; "Oxidation property of silicon small particles", *Appl. Phys. Lett.* **1991**, 58, 1662-1663.

18. Wolkin, M.V.; Jorne, J.; Fauchet, P.M.; Allan, G.; Delerue, C.; "Electronic States and Luminescence in Porous Silicon Quantum Dots: The Role of Oxygen", *Phys. Rev. Lett.* **1999**, *82*, 197-200.

19. Zhou, Z.Y.; Brus, L.; Friesner, R.; "Electronic Structure and Luminescence of 1.1- and 1.4-nm Silicon Nanocrystals: Oxide Shell versus Hydrogen Passivation", *Nano Letters* **2006**, *3*, 163-167.

20. Hua, F.J.; Erogbogbo, F.; Swihart, M.T.; Ruckenstein, E.;"Organically Capped Silicon Nanoparticles with Blue Photoluminescence Prepared by Hydrosilylation Followed by Oxidation" *Langmuir* **2006**, *22*, 4363-4370.

21. Credo, G.M.; Mason, M.D.; Buratto, S.K.; "External quantum efficiency of single porous silicon nanoparticles", *Appl. Phys. Lett.* **1999**, *74*, 1978-1980.

22. Buriak, J.M.; "Organometallic Chemistry on Silicon and Germanium Surfaces", *Chem. Rev.* **2002**, *102*, 1271-1308.

23. Bley, R.A.; Kauzlarich, S.M.; "A Low-Temperature Solution Phase Route for the Synthesis of Silicon Nanoclusters", *J. Am. Chem. Soc.* **1996**, *118*, 12461-12462.

24. Heath, J.R.; "A Liquid-Solution-Phase Synthesis of Crystalline Silicon", *Science* **1992**, *258*, 1131-1133.

25. Aihara, S.; Ishii, R.; Fukuhara, M.; Kamata, N.; Terunuma, D.; Hirano, Y.; Saito, N.; Aramata, M.; Kashimura, S.; "Electroreductive synthesis and optical characterization of silicon nanoparticles", *J. Non-Cryst. Sol.* **2001**, *296*, 135-138.

26. Fogler, H. S. *Elements of chemical reaction engineering* **2005**, 3rd ed, Prentice-Hall, New Jersey.

Chapter 4: Silicon nanocrystal size measurements

4.1 Introduction

I report a combined study of small angle neutron scattering (SANS) and high resolution transmission electron microscope (HrTEM) to investigate the size distribution of fluorescent silicon nanoparticles (SNs). SANS and TEM studies show good agreement and confirm the very small size particles and their distribution.

4.2 Silicon nanocrystal size measurements

4.2.1 Initiatives of studying size distribution

SNs prepared by the method described elsewhere [1][2] have a large size distribution. Because their sizes are within few nano meter range (<5nm), general methods of measuring particle's concentration (gravimetry, dynamic light scattering etc.) become inadequate or must be highly sensitive Small angle neutron scattering (SANS) study is a well developed and highly recognized method to study small polymer particle's physical and chemical characteristics [3]. It may also be applied to study inorganic particles.

4.2.2 SANS study of Si nanocrystal

With SANS, Botti et al. obtained size information and sitribution [4][5] of Si nanoparticles produced by laser abrasion of silane. Their TEM and SANS results show good mutual agreement for relatively large particles (>5 nm in diameter). However, lower resolution of TEM could not confirm the very small particles (<5

nm) which were calculated from SANS size distribution [4][5]. Furthermore, the laser abrasion methods of making Si nanoparticles are known to generate slightly clogged particles and usually result in average particles sizes exceeding 10 nm. Because of that their particles require further treatment to reduce sizes [6]. I study very small (below 5 nm in diameter) Si particle's sizes and population by independent methods.

4.3 Experimental section

4.3.1 Synthesis and functionalizing of Si nanocrystal

Silicon wafers (<111> oriented, 0.001~0.01 ohm-cm, As doped) were purchased from Virginia Semiconductor, Inc., Fredericksburg VA. Wafers were electrochemically etched in a HF: H_2O: Ethanol (2:1:1, volume ratio) mixture using the lateral etching method [7]. Anodic etching was performed in a polycarbonate cell that accommodates a 100 mm dia Si wafer placed between two Pt wire mesh cathodes. Electric contact was provided to the top edge of the vertically mounted wafer and electrolyte was slowly pumped into cell, hence providing a moving electrolyte boundary. Total etch time typically was about 4 h per 100 mm dia wafer at 120 mA constant current, supplied by a galvanostat (Model 363, EG&G Inc., Princeton, NJ). Following anodic etching, wafer is washed with copious amount of deionized water, methanol (HPLC grade, Mallinckrodt Chemicals, Phillipsburg, NJ) and blow-dried with nitrogen gas. Dried wafers displayed an intense orange-red luminescence when excited by a 360 nm UV lamp. Next, Si wafers were sonicated (Ultrasonik, York, PA) in deaerated 10:1(v:v) mixture of toluene and 1-octene for two hours under vigorous N2 purging. Resulting suspension appeared orangish and exhibited weak broadband

PL under UV excitation. After sonication, 20 ml of the Si nanoparticle suspension was delivered into the qualtz covette (Rayonet, Connecticut) with vigorous N_2 purging and placed inside the UV reactor (RMR-600, Rayonet, Connecticut) for photo-driven alkyl termination on the silicon nanoparticle. After 30 min UV reaction, 1-octene covered SNs shined with whitish color. Next, the sample was filtered through a silica gel column and the blue emitting portion was collected and completely dried with vacuum and N_2 purging. Deuternated cyclohexane was introduced to redisperse the dried Si particles. After reconstitution of the silicon nanoparticles, the sample fluoresced in bluish color.

4.3.2 SANS measurement

SANS measurement is performed with the NG-3 (30m) SANS instrument at National Institute of Standards and Technology. A description of the NG-3 beam line is found elsewhere [8]. Wave vectors from 0.003 to 0.45 $Å^{-1}$ correlated to the structural sizes ranging from around 10 Å to 5000 Å. Next, 1 ml of 1-octene derivatized silicon nanoparticles in deuternated cyclohexane was delivered to the 1 mm qualtz cell at room temperature. Measured scattering data was corrected for empty cell and blocked beam scattering. The SANS intensity was then rescaled to an absolute scale in units of cm^{-1}. Next, the Q-dependent macroscopic cross section is obtained by the radial averaging for isotropic scattering. Finally, scattering intensity, I, was plotted against the scattering vector, Q.

4.3.3 SANS data analysis

SANS data reduction and analysis were performed with IGOR software product (Wavemetrics, OR) [9]. The SANS data reduction macros are applied from the available database at NIST Center for Neutron Research (NCNR) [10] and appropriate models for Si nanoparticle are implemented.

4.3.4 HrTEM measurements

SNs prepared above were deposited on a TEM carbon grid (Tedpella, CA). High resolution TEM is measurement is performed with JEM2100F (JEOL, Tokyo, Japan).

4.3.5 Column chromatography and PL measurements

Silica gel, 200 mesh, (Sigma-Aldrich, MO) was used to separate 1-octene terminated SNs based on size. Subsequently, 1-octene terminated SNs were completely dried with N_2 gas and redispersed in tetrahydrofuran (THF). A Mixture of THF and cyclohexane (3/1, v/v) (Sigma-Aldrich, MO) was introduced as the mobile phase. UV lamp (model UVLS-26, UVP, CA) with 360 nm excitation was positioned along the separation column to trace the SNs. SNs' photoluminescence spectrum was recorded with a spectrofluorimeter (model LM800, SLM Inc., NY).

4.4 Results and Discussion

4.4.1 Summary of results

By applying Guinier and Porod's approximation [3], we estimated the mean radius of our Si nanoparticle sample. From the lognormal distribution model, we

predicted the size distribution of Si nanoparticles by fitting the modeling curve to the scattering intensity versus scattering vector graph obtained from SANS measurement on the same sample. HrTEM of the same sample shows almost monodispersed, spherical shaped SNs whose diameters are less than 5 nm. I estimated the concentration of Si nanoparticles from the TEM images and compared the size histogram to the size distribution curve from SANS data. Photoluminescence confirms the blue fluorescence of the Si nanoparticles.

4.4.2 Guinier approximation for low Q

In a low-Q range of scattering vector, Guinier law explains SANS data [3]~[5][11]. In case of the spherical shape of sample, Guinier law is described as:

$$\ln\left(\frac{d\Sigma}{d\Omega}\right) \approx \ln\left[\left(\overline{\rho}_{bd} - \overline{\rho}_{bm}\right)^2 C_p \frac{1}{6}\pi D^3\right] - \frac{Q^2 D^2}{20} \qquad (4.1)$$

where $\left(\overline{\rho}_{bd} - \overline{\rho}_{bm}\right)^2$ is the contrast factor which is the square of the difference of solvent and particle's scattering length density, C_p is the volume fraction, D is the diameter. From the slope of the curve between the logarithm of scattering intensity and the square of scattering vector, mean diameter D is retrieved and also volume fraction C_p is obtained.

With the results of Guinier approximation, I obtained parameters that characterize the size distribution of the sample. Then, I chose a model of size distribution that explains the SANS data.

Figure 4.1 shows the fitting on the low-q range of the SANS curve below q<0.04 from the result predicted by the Guinier approximation. IGOR software calculated the existing free parameters of the chosen distribution model, lognormal poly sphere

model, to predict the resulting size distribution curve (Fig. 4.2). Guinier approximation relates the scattering intensity and form factor of the sample for several shapes [12]. Although the spherical shaped sample generates a plateau at the low-q region ($qR_g<1$, where R_g is the radius of gyration) on the I vs. Q curve [12][13], our Si nanoparticles show a slope of -1, which means the sample is cylindrical in shape because of the following possibilities. First, since our method of particle production could inevitably produce large particles (>few micron) with irregular shapes, the resulting SANS data could show this behavior at low Q region. From the HrTEM study below (Fig. 4.6), even small particles are a perfectly spherical. Therefore the shape factor of neutron scattering represented the mean value of several possible geometries. Consequently, the plateau at low q region was absent. Second, these larger particles tend to weigh heavily [3][11], they significantly impact the SANS data although their number is much less than smaller particles. Third, the attractive force between spherical particles depress the slope at low q [14][15], because the surface of the 1-octene covered Si particles are not perfectly terminated to repel each other. It has been reported that only 45% of the Si surface [16] is covered with alkenes from photo driven alkylation.

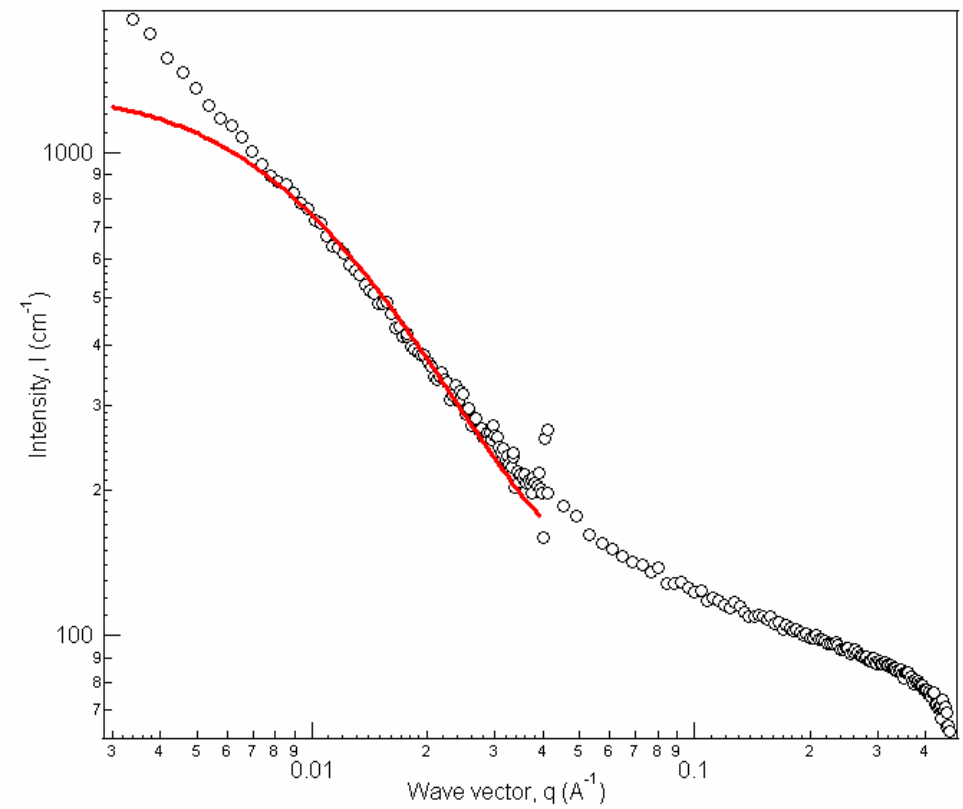

Figure 4.1. Model fitting on the low-q region of scattering cross section versus scattering wave vector obtained from SANS measurement. Lognormal poly sphere model has been implemented with predicted parameters from Guinier approximation,

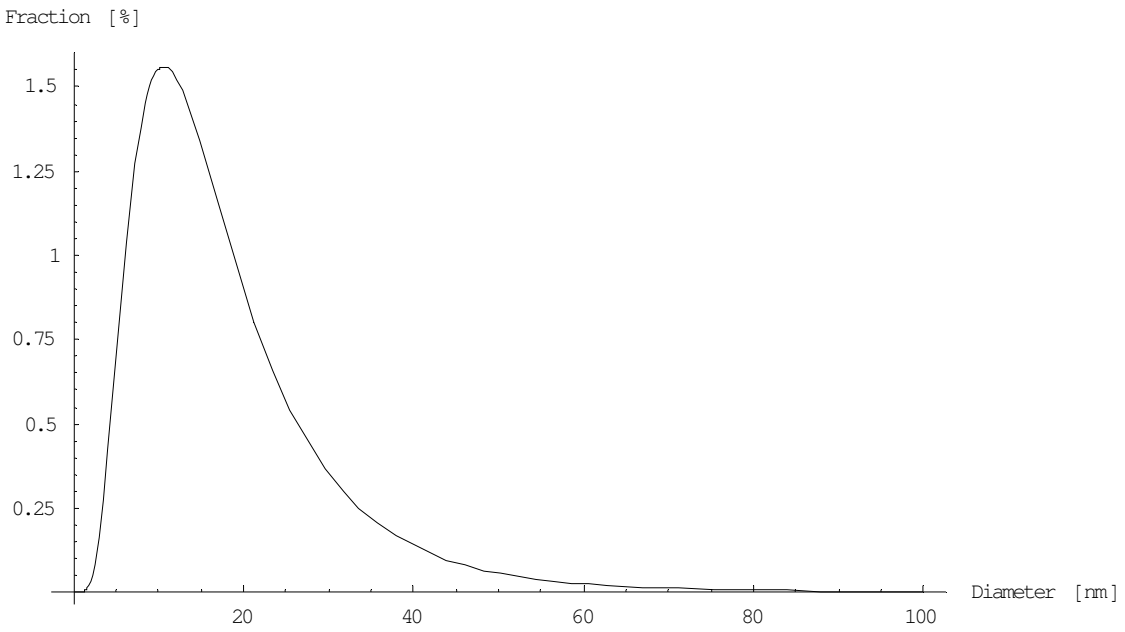

Figure 4.2 Size distribution curve from the model fitting of SANS data on the low-q range (0.001<q<0.04).

Therefore, the un-alkylized surface region of the Si nanoparticles could affect the balance of the attractive and repeulsive forces among particles, resulting in a decreased slope of I vs. Q at low-q range. Finally, the "wall effect" could additionally affect the slope in the low-q range of the I vs. Q curve [14][15]. Particles on a sample glass wall produce multiple scattering and lead to a strong up-lifting of the scattering curve at low-q range [14]. In our SNs, micron-sized aggregates of nanoparticles near sample cell's wall could be another factor that affects the low-q.

4.4.3 Porod approximation for high Q

At a high-Q range, Guinier law could no longer be applied [3]. At large values of Q, Porod law (Eq. (4.2)) is usually introduced to analyze the SANS data.

Before applying Porod law, background of the sample is subtracted by using a slope from the curve of $Q^4\left(d\sum/d\Omega\right)$ against Q^4 to correct for background noise which adversely effects SANS data at high-Q region [3]. Subsequent analysis with Porod approximation determines the possible mean diameter and volume fraction of a SNs sample.

$$\ln\left(\frac{d\Sigma}{d\Omega}\right)\approx \ln\left[\frac{12\pi C_p\left(\overline{\rho}_{bd}-\overline{\rho}_{bm}\right)^2}{D}\right]-4\ln Q \qquad (4.2)$$

A logarithmic plot of scattering cross section ($d\Sigma/d\Omega$) versus scattering wave vector (Q) shows a characteristic slope of -4 as indicated in Eq. (4.2), and its y intercept is related to the diameter (D) and volume fraction (Cp) of the spherical particles. With a mean diameter (~3.1 nm) obtained from the HrTEM study, the only free variable left was volume fraction, which was subsequently calculated from the value of y intercept.

Fig. 4.3. shows the high-Q fitting (q range, 0.05~0.3 Å) of the scattering cross section vs. scattering wave vector curve based on the parameters estimated from the Porod approximation. Figure 4.4 depicts the size distribution curve generated from the fitting result of SANS data at high q-region (q>~0.04 Å). Since neither Guinier nor Porod approximation alone explains the entire q range, it is better to combine two approximations to explain SANS results [3]. Figure 4.5 shows the comparison of the size distribution resulted from the two approximations.

4.4.4 Hr-TEM results

HrTEM study (Fig. 4.6.) shows almost monodisperse particles with diameters ranging 2~5 nm. A histogram of the HrTEM results (Fig. 4.7.) obtained with the image analysis toolkit from Matlab (the Mathworks, Natick, MA) shows the distribution of particles with a mean diameter of 3.1 nm. The SANS fitting results (Fig. 4.4.) at high-q and the HrTEM results (Fig. 4.7.) both shares a similar mean diameter and distribution of the Si particles.

4.4.5 Fluorescence spectra of Si nanocrystal

Fluorescence spectrum of SNs is another indirect means of accessing the nanoparticle's size. PL profiles have previously been reported on different sized SN preparations (for a summary see [17]).

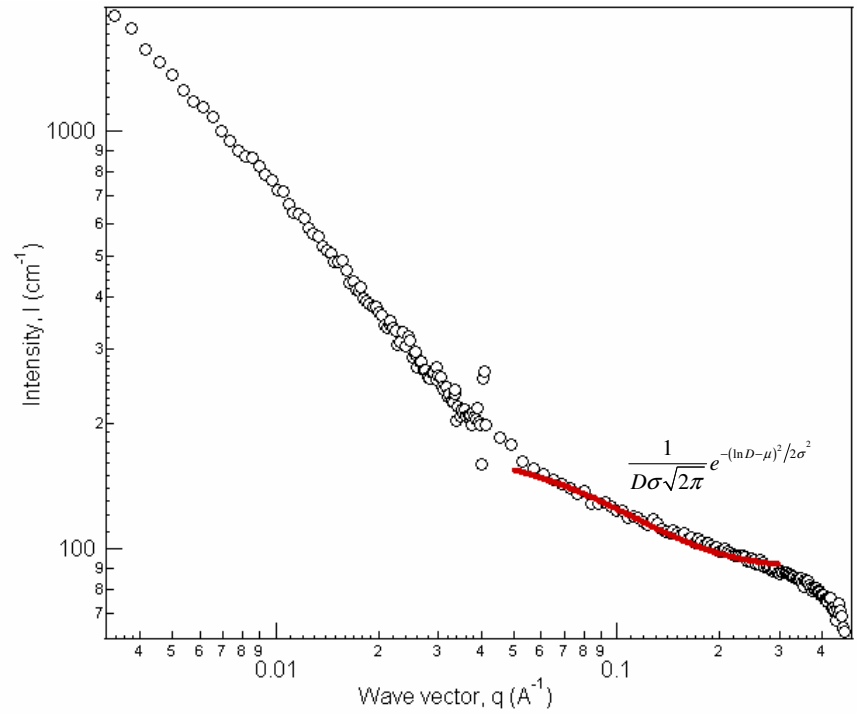

Figure 4.3 Model fitting of scattering cross section versus wave vector curve focused on the high-q region ranging from 0.04 to 0.3 Å.

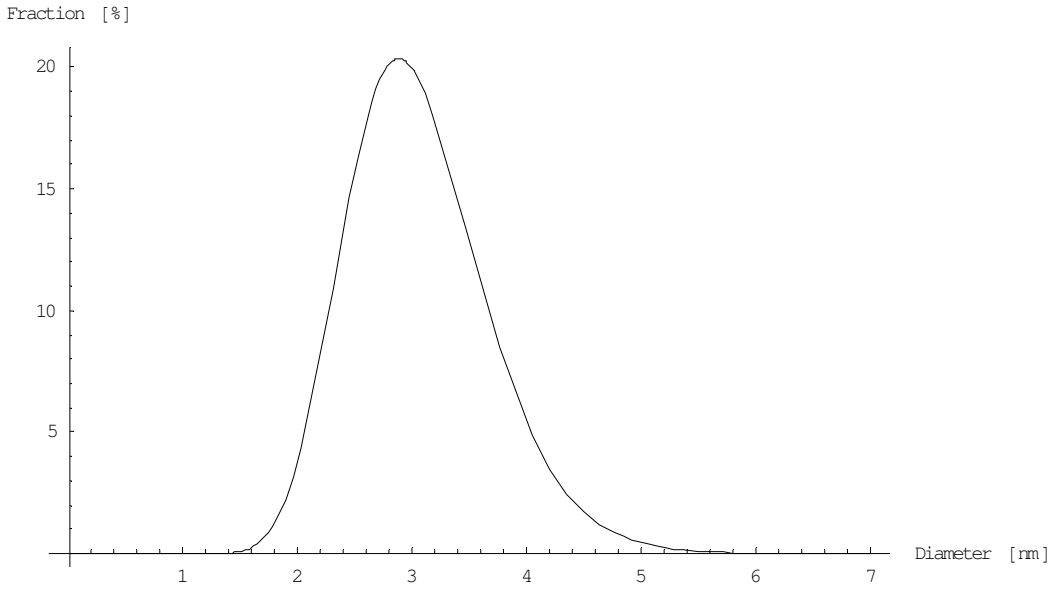

Figure 4.4 Calculated distribution curves from model fitting of SANS data with lognormal poly sphere distribution.

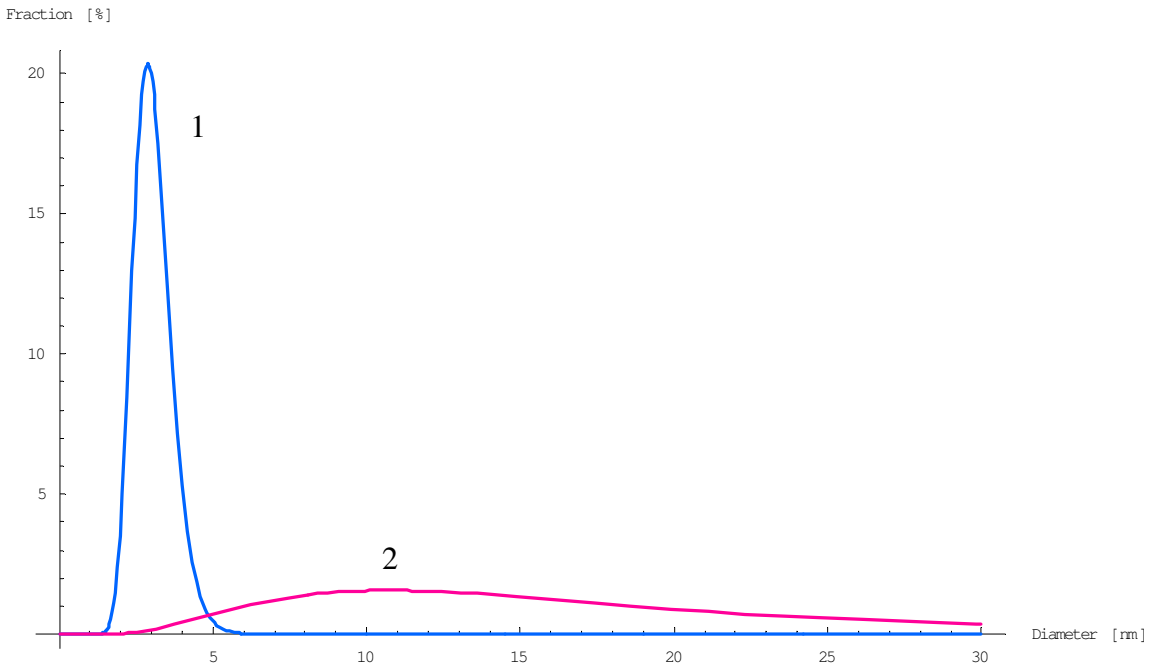

Figure 4.5 Size distribution curve produced from the SANS fitting. (1) high-q region (0.04<q<0.3 Å) fitting. (2) low-q region (0.001<q<0.04 Å) fitting.

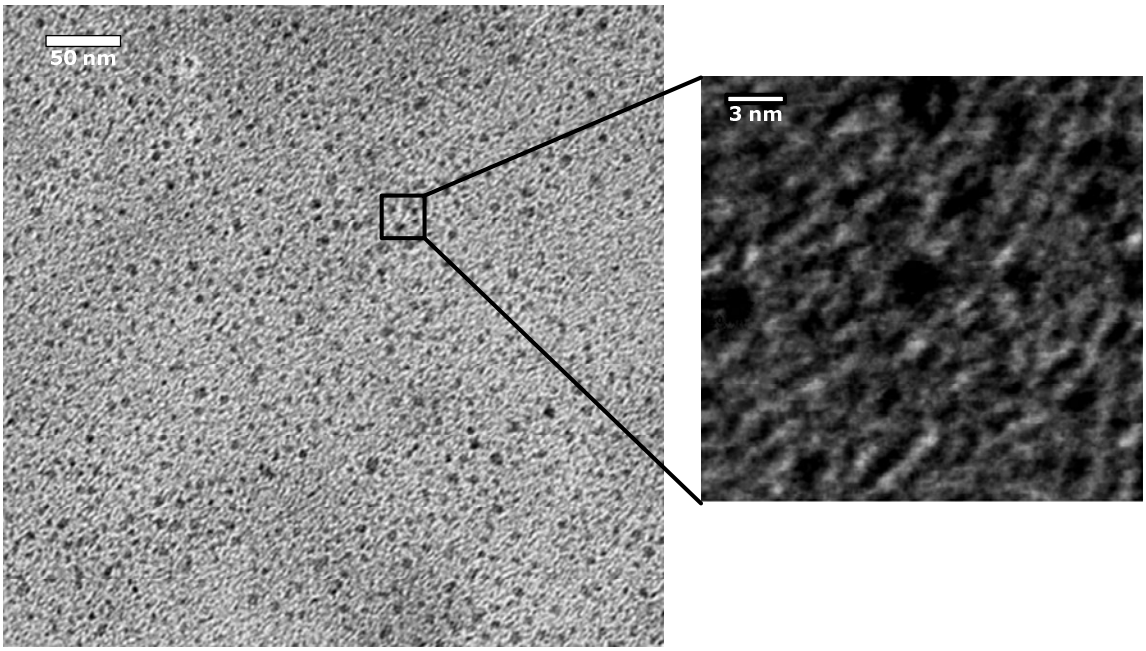

Figure 4.6 HrTEM result of 1-octene derivatized silicon nanoparticles. Onset is the magnification of the photo which clearly shows the various sizes of Si nanoparticles.

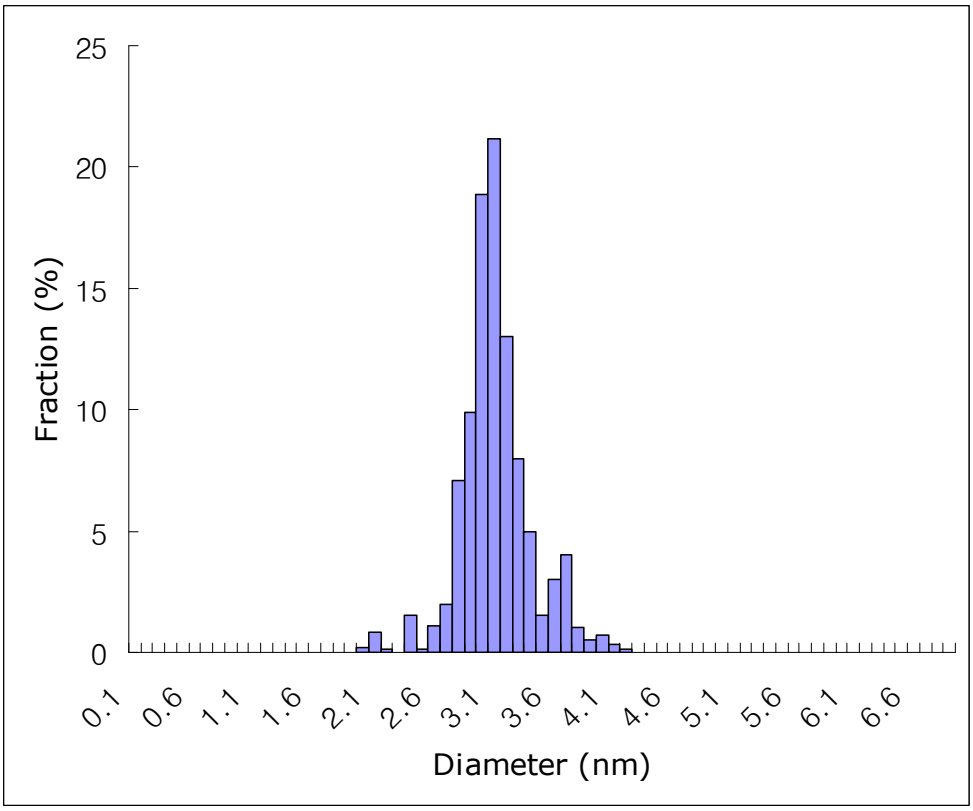

Figure 4.7 Histogram of the Silicon nanoparticle obtained from the image analysis of high resolution TEM results.

From the fluorescence measurement of our SNs, we infer a broad distribution of SNs ranging from 1 to 5 nm in diameter. This corresponds to emission in the blue to red visible spectrum (Fig. 4.8). Column chromatography can be utilized to separate SNs according to theirs size differences [16]. Figure 4.8a shows a broad band of SNs mostly shining in blue and red. Light brownish particles remaining at the top of the separation column, was hinted by the existence of the larger aggregates of SNs.

4.4.6 Optical transmission spectra

Optical transmission spectra correlate to the size distribution of silicon particles in porous silicon film [18]. Figure 4.9 shows the transmission spectrum of 1-octene terminated silicon nanoparticles and the corresponding size distribution curve.

4.5 Summary

I studied SANS on silicon nanoparticles with mean diameters ranging from 2~5 nm. SANS yields information on size, shape and population of inorganic Si nanoparticles. HrTEM study supports the particle diameter and population deduced from SANS data. Indirect evidences of size distribution were also investigated with optical fluorescence and transmission spectra. They all confirm the size distribution of the silicon nanoparticles to be within th nanometer range determined with HrTEM and SANS. Further studies are warranted to explain relationship between the slope of I vs. Q curve at low q region and particle's physical and chemical characteristics (shape factor, attractive or repulsive force and surface chemical compositions).

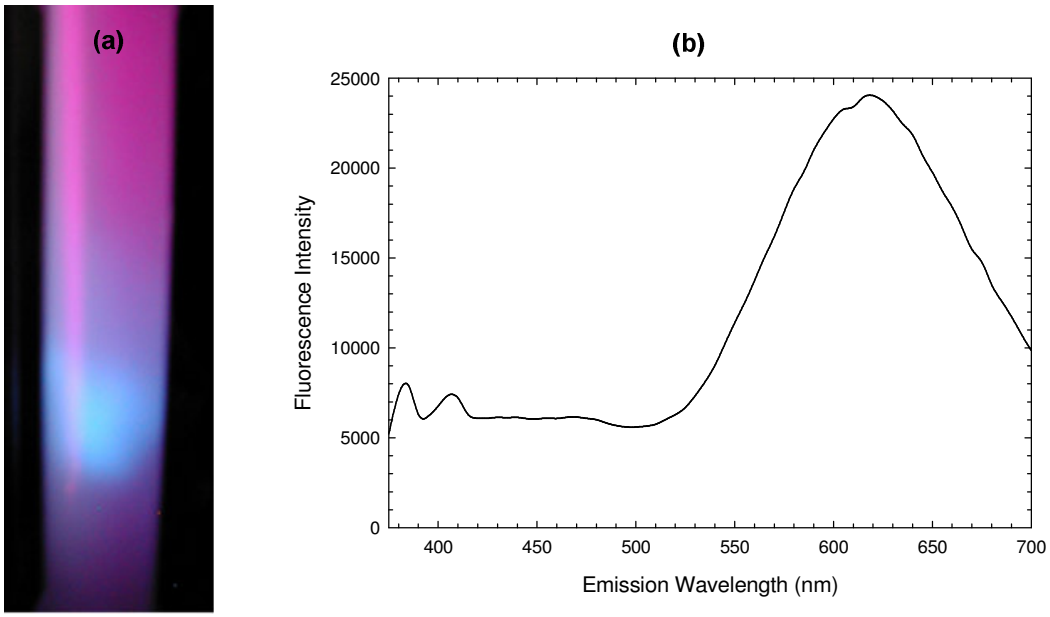

Figure 4.8 Column chromatography and fluorescence spectrum of 1-octene terminated SNs. (a) Silica gel column separates SNs based on size. (b) Fluorescence measurement on SNs with 360 nm excitation wavelength.

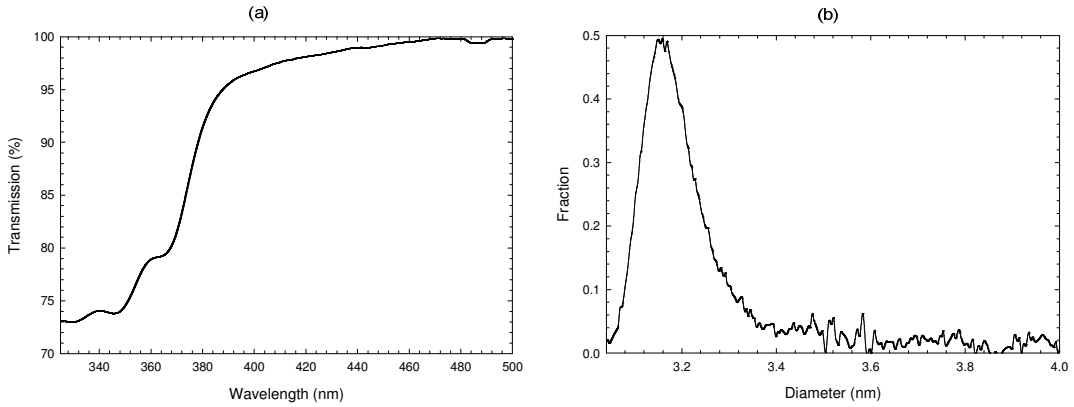

Figure 4.9 Optical transmission spectrum,(a) and resulted size distribution curve, (b).

4.6 References

1. Wang, L.; Reipa, V.; Blasic, J. "Silicon Nanoparticles as a Luminescent Label to DNA", *Bioconjugate Chem.* **2004**, *15*, 409-412.
2. Choi, J.; Wang, N. S.; Reipa, V.; *Langmuir*, in revision.
3. Skőld, K.; Price, D. L. *Methods of Experminetal Physics: Neutron Scattering* **1987**, 23, part C, Academic Press, Florida.
4. Botti, S.; Coppola, R.; Gourbilleau, F.; May, R. P.; Rizk, R.; Valli, M. "SANS and TEM investigation of laser-synthesized photoluminescent Si nanoparticles", *Appl. Phys. A* **2002**, *74*, s1230-s1232.
5. Botti, S.; Coppola, R.; May, R. P.; Valli, M. "Photoluminescence properties and size distribution in laser synthesized Si nanopowders for optoelectronic devices", *J. Appl. Cryst.* **2003**, *36*, 632-635.
6. Li, X.; He, Y.; Talukdar, S. S.; Swihart, M. T. "Process for Preparing Macroscopic Quantities of Brightly Photoluminescent Silicon Nanoparticles with Emission Spanning the Visible Spectrum", *Langmuir*, **2003**, *19*, 8490-8496.
7. Jung, K. H.; Shih, S.; Hsieh, T. Y.; Kwong, D. L.; Lin T. L. "Intense photoluminescence from laterally anodized porous Si", *Appl. Phys. Lett.* **1991**, *59*, 3264-3266.
8. Glinka, C. J.; Barker, J. G.; Hammouda, B.; Krueger, S.; Moyer, J. J.; Orts, W. J. "The 30 m Small-Angle Neutron Scattering Instruments at the National Institute of Standards and Technology", *J. Appl. Cryst.* **1998**, *31*, 430-445.
9. Kline, S. R. "Reduction and analysis of SANS and USANS data using IGOR Pro", *J Appl. Cryst.* **2006**, *39*, 895-900.

10. http://www.ncnr.nist.gov/programs/sans/data/data_red.html
11. Roe, R. *Methods of X-Ray and Neutron Scattering in Polymer Science* **2000**, Oxford University Press, New York.
12. Hubbard, F. P, Jr.; Santonicola G.; Kaler, E. W.; Abbott, N. L. "Small-Angle Neutron Scattering from Mixtures of Sodium Dodecyl Sulfate and a Cationic, Bolaform Surfactant Containing Azobenzene", *Langmuir* **2005**, 21, 6131-6136.
13. Brasher, L. L. ; Kaler, E. W.; "A Small-Angle Neutron Scattering (SANS) Contrast Variation Investigation of Aggregate Composition in Catanionic Surfactant Mixtures", *Langmuir* **1996**, *12*, 6270-6276.
14. Innerlohinger, J.; Wyss, H. M.; Glatter, O. "Colloidal Systems with Attractive Interactions: Evaluation of Scattering Data Using the Generalized Indirect Fourier Transformation Method", *J. Phys. Chem. B* **2004**, *108*, 18149-18157.
15. Innerlohinger, J. ; Villa, M.; Baron, M.; Glatter, O. "Ultra-small-angle neutron scattering from dense micrometre-sized colloidal systems: data evaluation and comparison with static light scattering", *J. Appl. Cryst.* **2006**, *39*, 202-208.
16. Hua, F.; Swihart, M. T.; Ruckenstein, E. "Efficient Surface Grafting of Luminescent Silicon Quantum Dots by Photoinitiated Hydrosilylation", *Langmuir* **2005**, *21*, 6054-6062.
17. Wilcoxon, J.P.; Samara, G.A.; Provencio, P.N.; "Optical and electronic properties of Si nanoclusters synthesized in inverse micelles", *Phys. Rev. B.* **1999**, *60*, 2704-2714.
18. Fonseca, L.F.; Resto, O.; Gupta, S.; Katiyar, R.S.; Weisz, S.Z. *Proc. Of the 24th ICPS* **1999**, D. Gershoni ed., World Scientific.

Chapter 5: Surface modification of silicon nanocrystal

5.1 Introduction

Hydrocarbon chains on the surface of nanoparticles render the nanoparticles strongly hydrophobic and they repel each other in a solution resulting in a monodispersed Si nanocrystal suspension. In this study, I investigate optical characteristics of alkene passivated silicon nanocrystals. I explore the effect of the alkene chain length on the optical properties of Si nanocrystals. Si nanocrystals are first synthesized from the anodic etching of Si wafers and mechanical stripping of the porous surface layer from the etched wafers. Photo-catalysis with 250 nm UV light promotes surface modification of hydrogen terminated Si nanocrystals with selected alkenes through hydrosilylation. When observed under visible light, turbid and brownish particle suspension turns to a clear solution after 30 min of photo reaction. Also, red emitting Si nanocrystals turn bright blue under 360 nm UV light excitation. The resulting fluorescent Si nanocrystals with alkene modified surface were characterized with photoluminescence spectroscopy, high resolution transmission electron microscope, absorption spectroscopy, and time resolved fluorescence spectroscopy. Surface alkylation results in photoluminescence peaks shifting to both higher energy levels (shorter wavelength) and higher intensity while photoluminescence peaks of different alkene modified Si NCs reflect variation in exciton lifetime. Quantum efficiency of Si nanocrystals decreases with increasing alkene carbon chain length. Photoluminescence decay lifetime of alkene passivated Si

NCs are all in the nano-second range, indicating direct inter band transitions. Further research on photoluminescence efficiency and particle stability dependence on passivating shell composition of our Si nanocrystals would facilitate biomedical applications of silicon nanoparticle

5.2 Passivation of silicon nanocrystals with alkenes

5.2.1 Merits of Si nanocrystal surface modification

Bare silicon nanocrystals often require surface modification because of bare particles' weak Si-H bonds. In an open environment, bonds between silicon and hydrogen are rapidly exchanged with more stable silicon-oxide bond. Also, bare silicon nanocrystal is subject to aggregation among particles. Surface modification of nanocrystal helps prevent natural oxidation resulting from exposure to air and provides stable, well dispersed particles. More importantly, functionalized Si nanocrystals with different functional groups could provide a platform for further applications of Si nanocrystals. Table 5.1 summarizes the different functional groups and characteristics of modified Si nanocrystals.

	Functional Groups	Solvents	Characteristics
More Hydrophobic	-CH3	Alkenes	stable suspension
	-CH2	Styrene	efficient covering
	-H	Bare particle	unstable
	-OH	Alcohol	less stable
More Hydrophilic	-COOH	Acrylic Acid	water soluble
	-NH2	Allylamine	water soluble

Table 5.1 Functional groups on a surface of Si nanocrystal and characteristic properties.

5.2.2 Theoretical modeling of alkene chain length on the optical properties

Reboredo et. al. studied the band gap changes along with a different alkene chains on a surface of silicon particles [1]. One of their interesting findings was that the energy gaps between the highest occupied molecular orbital (HOMO) and the lowest unoccupied molecular orbital (LUMO) of carbo-hydro modified Si nanocrystals have a tendency to fluctuate with the number of carbons in a carbo-hydro chain. Figure 5.1 shows the simulation results on the HOMO-LUMO gaps of different Si clusters as a function of the passivation of the Si nanocrystals' surface. In my study, I varied the number of carbons in carbo-hydro chains on Si nanocrystal surface from 6 (1-hexene) to 16 (1-hexadecene) and confirmed the effect of the number of carbons on and bandgap.

5.3 Experimental section

Figure 5.2 shows the overall procedure of synthesis and passivation of silicon nanocrystal. Silicon wafers (<111> oriented, 0.001~0.01 ohm-cm, As doped) were purchased from Virginia Semiconductor, Inc., Fredericksburg VA. Wafers were electrochemically etched in a HF: H_2O: Ethanol (2:1:1, volume ratio) mixture using the lateral etching method [2][3]. Anodic etching was performed in a polycarbonate cell that accommodates a 100 mm dia Si wafer placed between two Pt wire mesh cathodes. Electric contact was provided to the top edge of the vertically mounted wafer and electrolyte was slowly pumped into the cell, hence providing a moving electrolyte boundary. Total etch time typically was about 4 h per 100 mm dia wafer at 120 mA constant current, supplied by a galvanostat (Model 363, EG&G Inc., Princeton, NJ).

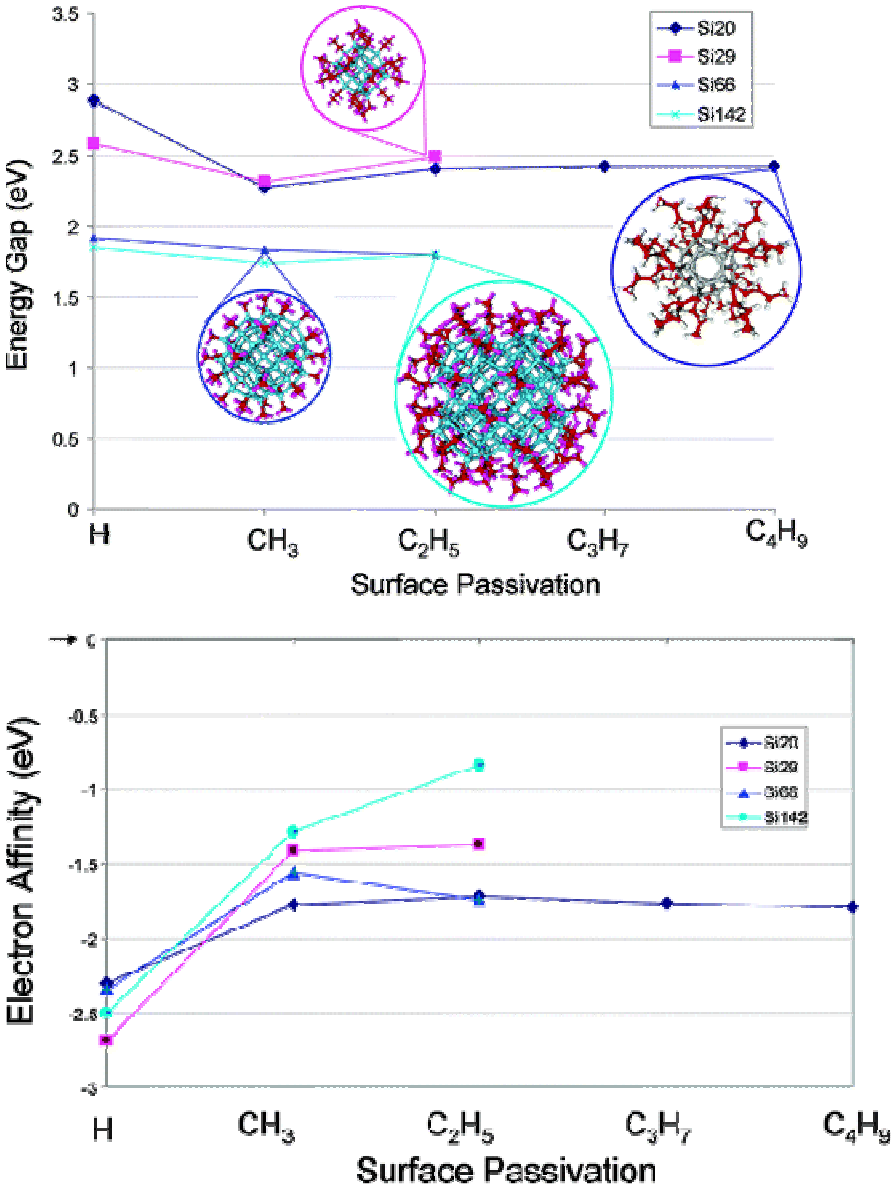

Figure 5.1 Simulation results of the effect of surface passivation on HOMO-LUMO bandgap energies. [1]

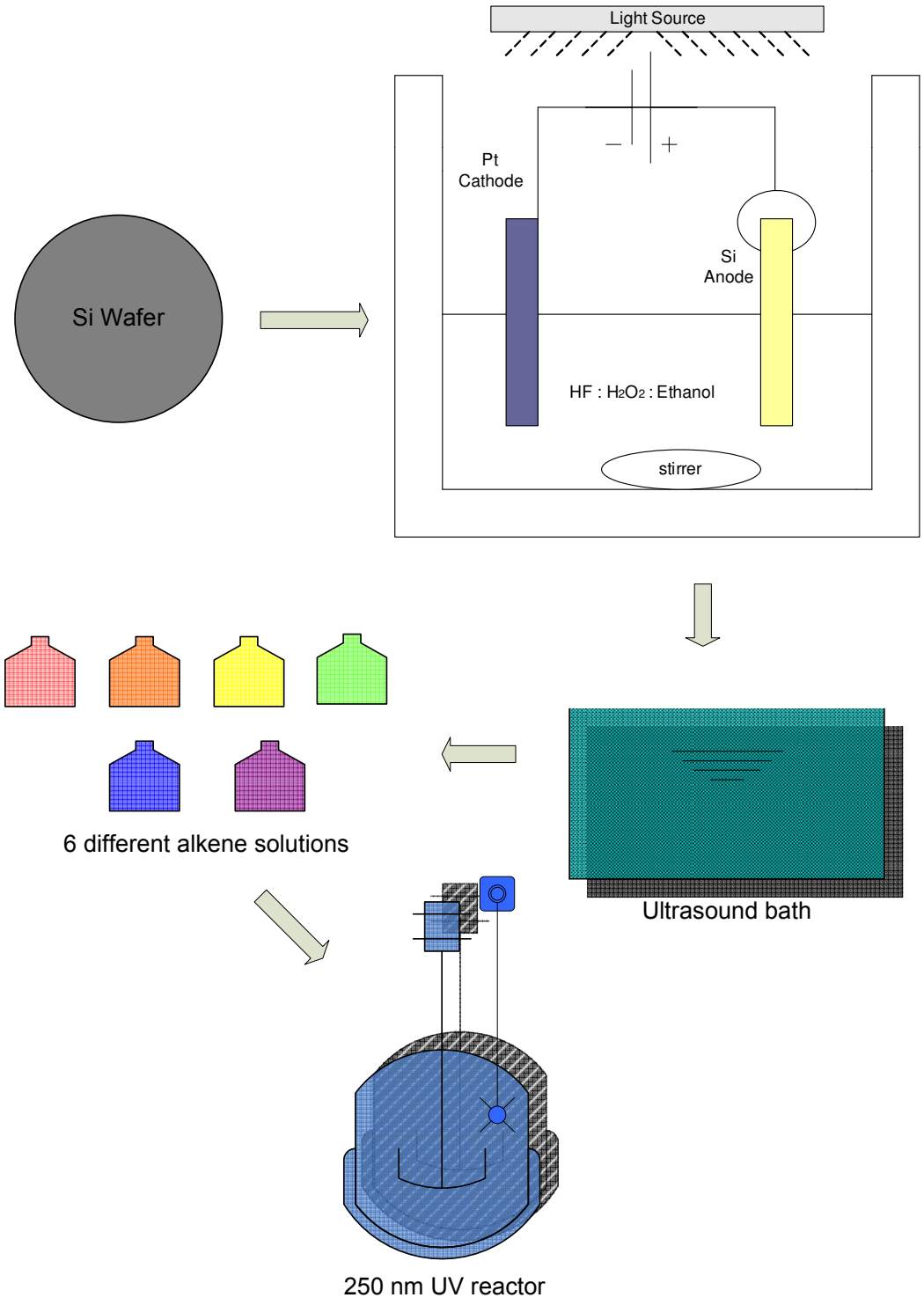

Figure 5.2 Overall process of synthesis and functionalization of silicon nanocrystals.

Following anodic etching, wafer is washed with copious amount of deionized water, methanol (HPLC grade, Mallinckrodt Chemicals, Phillipsburg, NJ) and blow-dried with nitrogen gas. Dried wafers displayed an intense orange-red luminescence when excited by a 360 nm UV lamp. Next, Si wafers were sonicated (Ultrasonik, York, PA) in deaerated 10:1(v:v) mixture of toluene for two hours under vigorous N_2 purging. Resulting suspension appeared orangish and exhibited weak broadband PL under UV excitation. After sonication, 20 ml of the Si nanoparticle suspension was delivered into a qualtz cuvette (Rayonet, Connecticut) with vigorous N_2 purging and placed inside a UV reactor (RMR-600, Rayonet, Connecticut) for photo-driven alkyl termination on the silicon nanoparticle. By adding 5 ml of each 6 different alkene solvents, 6 different batches of silicon nanocrystals were prepared and ready for UV reaction. After 30 min UV reaction, alkene covered SNs shined in different fluorescence color with different carbo hydro coatings on them. Next, samples were filtered through silica gel column to remove micron-sized aggregates.

5.4 Results and discussion

5.4.1 Fluorescence changes

250 nm UV light promotes surface modification of hydrogen terminated Si nanocrystals with selected alkenes through hydrosilylation reaction. Figure 5.3 compares fluorescence under UV excitation before and after alkene passivation. It shows a drastic shift of fluorescence and stronger fluorescent intensity with alkene passivation. Figure 5.4 shows the photoluminescence results from Si nanocrystal with and without 1-octene. Clearly it shows the emission peak shifting from 620 nm to 430 nm and excitation peak shifting from 390 nm to 340 nm.

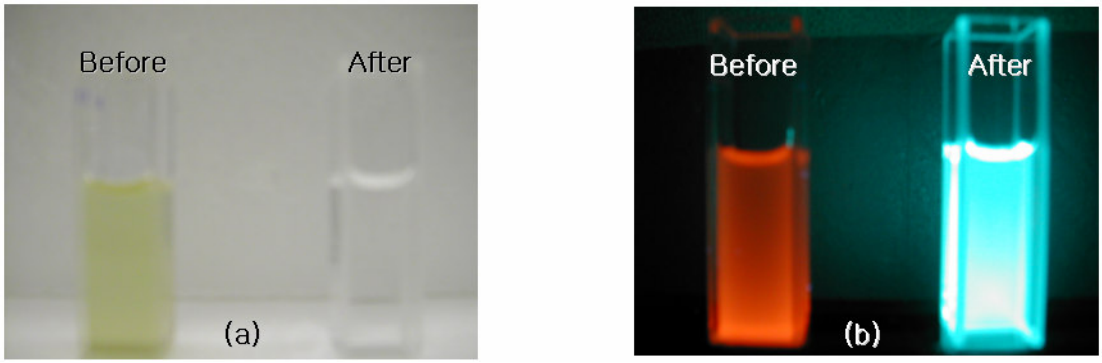

Figure 5.3 Comparisons of the effects on photoluminescence changes by surface modification. (a) Cuvettes containing carbo-hydro terminated sample (right) and untreated sample (left) under visible light. (b) Same cuvettes with (a) under 360 nm UV light.

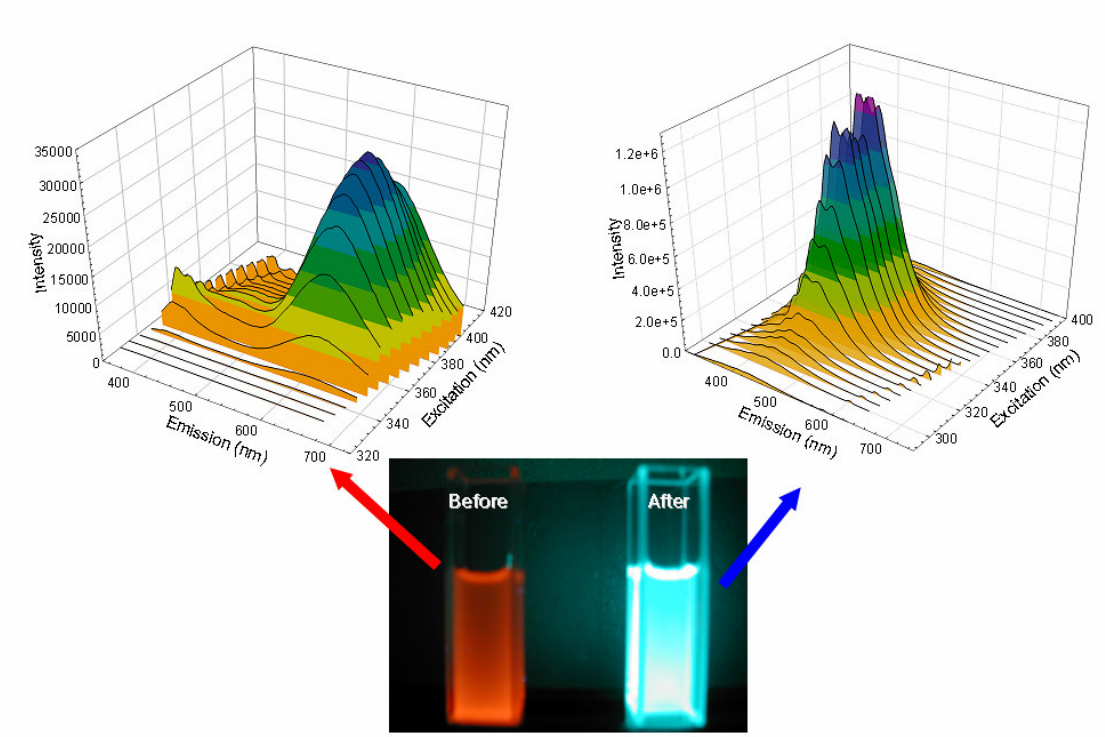

Figure 5.4 Photoluminescence shift of carbo-hydro termination on surface of Si nanocrystals.

5.4.2 PL peak shifting with surface modification

Figure 5.5 shows the different fluorescence from the different carbo-hydro modified silicon nanocrystals. All of the batches shifted toward bluish emission range, but there was a difference in terms of the degree of shifting. Fig. 5.6 shows the degree of peak shifting with the number of carbons in carbo-hydo chains on the surface of Si nanocrystal.

5.4.3 Quantum efficiency variation with surface modification

The quantum efficiency of these samples with different carbo-hydro coatings was measured. Quantum efficiency decreased with increasing alkene carbon chain length. Table 5.2 depicts the tendency of quantum efficiency dependence on carbo hydro chain length. Quantum efficiency of the Si NC referenced with respect to a well known conventional dye, quinine bisulfate. Under the same excitation intensity and instrumental conditions, one can assume that the fluorescence intensity ratio ($F_{sample}/F_{quinine}$) between the two solutions is proportional to the ratio of total rate of emission from them ($Q_{sample}/Q_{quinine}$) [4]. Also, in a dilute solution where one can ignore the excessive absorption of excitation light and self absorption of the sample, the rate of emission of fluorescence, Q, is defined as,

$$Q = I_o \varepsilon c l \phi$$

where I_o is the intensity of incident light, ε is molecular absorptivity, c is the constant velocity of light, l is the optical depth and ϕ is the absolute fluorescence efficiency. Therefore, the ratio of the fluorescence intensities between Si NC sample and quinine sulfate is described as,

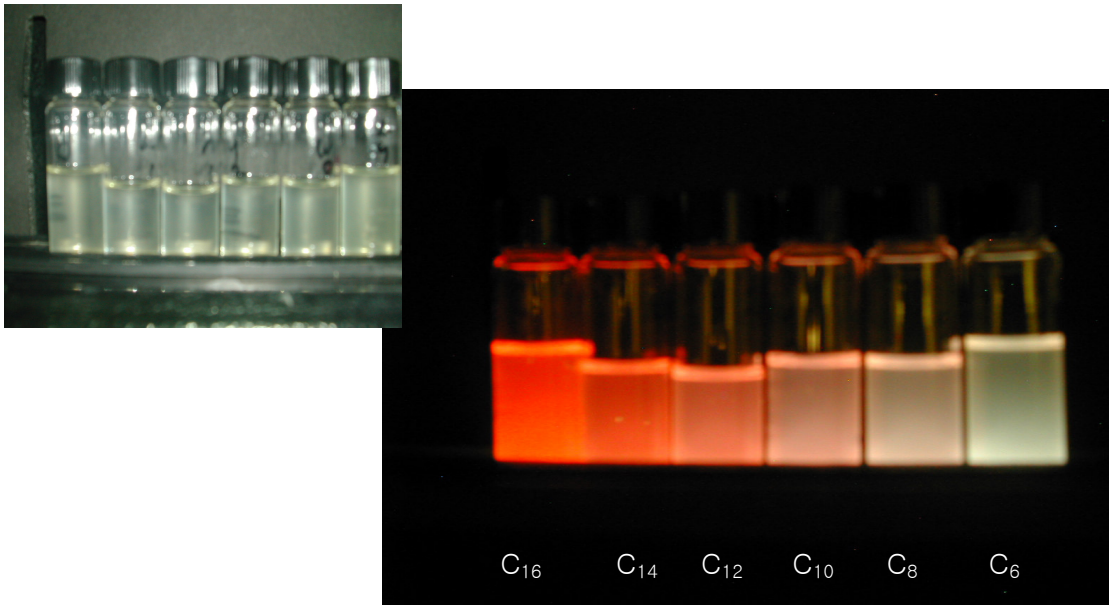

Figure 5.5 Different fluorescence from different carbo-hydro coated Si nanocrystals. On the left, same samples under visible light.

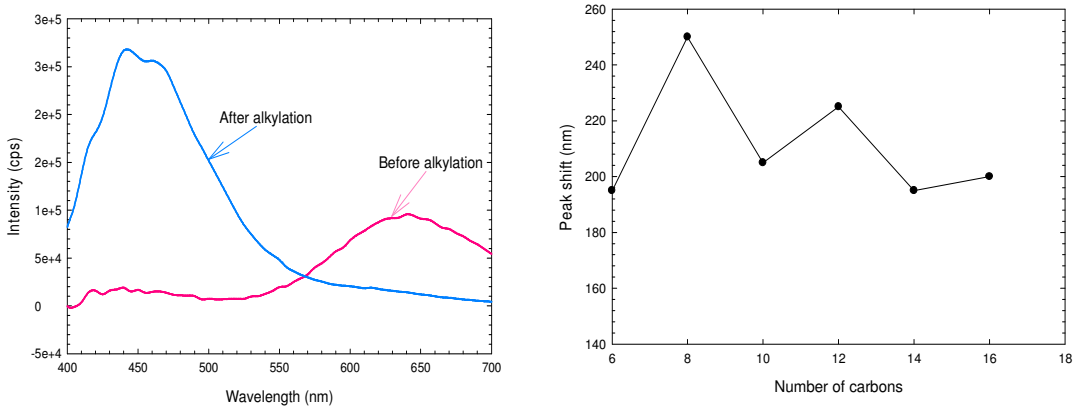

Figure 5.6 On the right, the degree of peak shifting from initial, bare Si nanocrystal photoluminescence to final, alkene terminated Si nanocrystal photoluminescence.

$$\frac{F_{SiNC}}{F_{quinine}} = \frac{Q_{SiNC}}{Q_{quinine}} = \left(\frac{\phi_{SiNC}}{\phi_{qunine}} \right) \frac{Optical\ density_{SiNC}}{Optical\ density_{quinine}}$$

Absolute quantum efficiency of quinine sulfate is known as 0.55 at 360 nm exciting wavelength [4]. From the optical densities measured in absorption spectrum and fluorescence intensities in photoluminescence spectrum, relative quantum efficiency of the Si NC (ϕ_{SiNC}) is obtained. Table 5.2 summarizes quantum efficiencies of Si NCs from the various visible emissions.

Alkene	QE
1-Hexene	67%
1-Octene	55%
1-Decene	29%
1-Dodecene	9.2%
1-Tetradecene	2.2%
1-Hexadecene	0.7%

Table 5.2 Quantum efficiency comparison among different alkene terminated Si nanocrystals.

5.4.4 Lifetime variation with surface modification

Figure 5.7 shows the decay measurement of Si nanocrystals covered with 1-octene. Three lifetimes are assumed and their mean values are compared among alkene terminated silicon nanocrystals in Table 5.3.

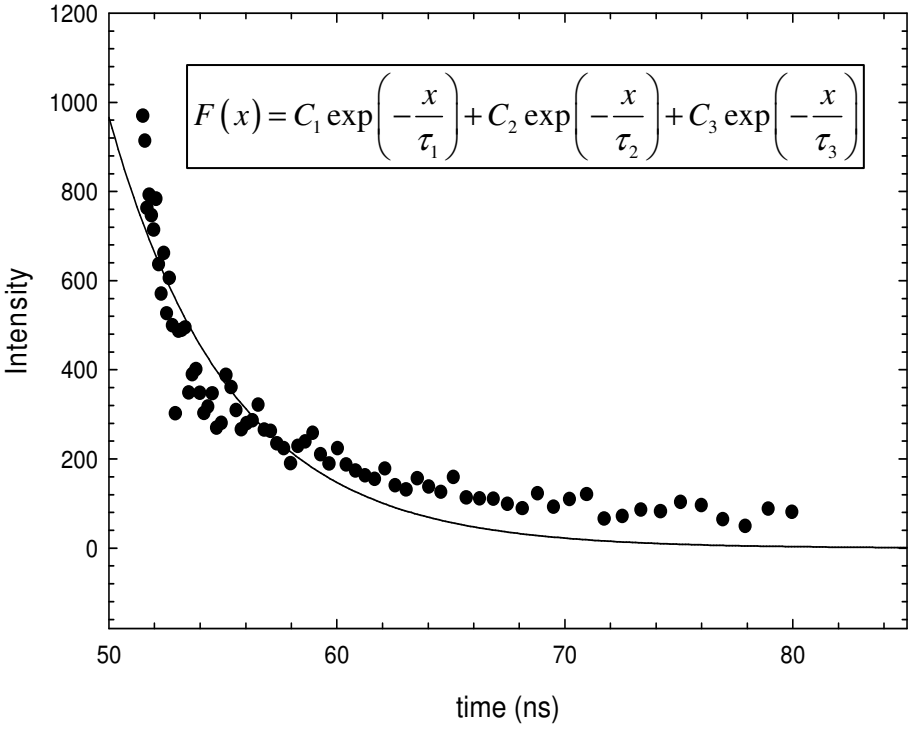

Figure 5.7 Decay time measurement of 1-octene covered Si nanocrystal. 3 parameters for decay time are applied.

Fluorescence lifetime measurement confirms that alkene passivated Si nanocrystals are all in the nano second range, indicating direct inter band transitions.

Alkenes on surface	Mean Life time (ns)
1-Hexene (C6)	5.10
1-Octene (C8)	2.77
1-Decene (C10)	3.14
1-Dodecene (C12)	3.02
1-Tetradecene (C14)	4.37
1-Hexadecene (C16)	3.88

Table 5.3 Mean life time comparison among different alkene terminated Si nanocrystals.

5.5 Summary

As predicted from theoretical studies, carbo-hydro surface modification clearly affects optical properties of silicon nanocrystals. Our experiment confirm the theoretically predicted relationship between carbo-hydro chain length and photoluminescence peak shift. Compared to H-termination, surface alkylation through UV-assisted hydrosilylation leads to higher quantum yield and significantly improves Si nanocrystal photoluminescence stability. Life time measurement suggests that blue emission after alkylation is consistent with direct radiative recombination in alkene passivated nanoparticles. From the quantum efficiency measurement,, an inverse relationship was observed between photoluminescence quantum yield and alkene chain length.

5.6 References

1. Reboredo, F.A.; Galli, G.; "Theory of Alkyl-Terminated Silicon Quantum Dots", *J. Phys. Chem. B.* **2005**, *109*, 1072-1078.
2. Wang, L.; Reipa, V.; Blasic, J. "Silicon Nanoparticles as a Luminescent Label to DNA", *Bioconjugate Chem.* **2004**, *15*, 409-412.
3. Choi, J.; Wang, N. S.; Reipa, V.; *Langmuir*, in revision.
4. Parker, C. A. *Photoluminescence of solutions* **1968**, Elsevier publishing company, Amsterdam.

Chapter 6: Silicon nanocrystal bio-conjugation

6.1 Introduction

Surface modification of silicon nanocrystals allows them to be conjugated to biomolecules. Since silicon nanocrystals are superior to organic dyes in terms of photostability and are smaller and potentially less cytotoxic than commercially available binary quantum dots, they could serve as the next generation fluorophores. I synthesized Si nanocrytals with high quantum yield, narrow size distribution that are ready to be bio conjugated. In this study, streptavidin is introduced as a target protein, and a succidimidyl based bi-functional crosslinker is used to bridge the 1-octene covered Si nanocrystal and the target protein. Conjugation of Si nanocrystals to streptavidin is observed through elution changes in native gel electrophoresis. Streptavidin conjugates of Si nanocrystals are promising candidates to further target a wide range of bio materials marked with biotin.

6.2 Bio conjugation strategies

6.2.1 Simple incubation of Si nanocrystals with the bio molecule

Simple incubation of Si nanocrystal with target biomolecules helps determine whether there is sufficient electrostatic force to attach theses nanoparticles to the target. I tried Si nanocrystals with surfaces that are either naturally, hydrophobic (alkyl terminated), or hydrophilic (thermally oxidized). Oxidized surface give rise to water solubility, thus accessible to biomolecules. Without any surface modification,

BSA protein is incubated with theses oxidized Si nanoparticles. Fluorescent level was maintained in both kinds of Si nanocrystals. However, there was no evidence that the conjugates are present.

6.2.2 Coupling through the surface functionalization

Surface modification of Si qdots with carboxyl or amine group termination has been reported by several groups [1][2]. Sato et al. treated H-terminated Si nanocrystals with acrylic acid to create carboxyl functional groups on a surface. Warner et al. reported depositing amine functional groups on surface of Si nanocrystals to make them suspendable in water. These approaches are examples of engineering desired functionality on silicon nanocrystals. More importantly, surface modification increases monodispersity of nanoparticles and decreases aggregation among particles, a specially serious issue in a nano scale.Beyond fabricating water soluble nanoparticles, we need to quantify the percentage of surface that is modified and the number of active functional groups on a particle.

6.2.3 Covalent linkage

Various approaches of conjugating nanoparticles to biomolecules have been reported [3]. In this study, I used 4-azido-2,3,5,6-tetrafluorobenzoic acid, succinimidyl ester (ATFB, SE) which is a bi-functional crosslinker that has a photo reactive arm and an amine reactive arm. The overall process of conjugating biomolecules to silicon nanocrystals is described in Figure 6.1. After H-terminated, bare Si particles are synthesized, their surface is terminated with carbo-hydro group and the ATFB bi-functional linker is introduced to cover the surface with groups that

can react with amines. Subsequently, the Si-succinimidyl ester conjugates are coupled with streptavidin to form a final bio conjugated product. Since the crosslinker has the UV reactive arm on one side, the reactive properties of the chemical and photoreactive groups determine whether the conjugates are couple like or unlike functional groups. Figure 6.2 shows a detailed view of conjugating a target protein to the nanoparticle by using ATFB crosslinker.

6.3 Experimental section

6.3.1 Si nanocrystal synthesis

Silicon nanocrystals are prepared with anodic etching of silicon wafer in HF based acidic solution. Silicon wafers (<111> oriented, 0.001~0.01 ohm-cm, As doped) were purchased from Virginia Semiconductor, Inc., Fredericksburg VA. Wafers were electrochemically etched in a HF: H_2O: Ethanol (2:1:1, volume ratio) mixture using the lateral etching method [5][6]. Anodic etching was performed in a polycarbonate cell that accommodates a 100 mm dia Si wafer placed between two Pt wire mesh cathodes. Electric contact was provided to the top edge of the vertically mounted wafer and electrolyte was slowly pumped into the cell, hence providing a moving electrolyte boundary. Total etch time typically was about 4 h per 100 mm dia wafer at 120 mA constant current, supplied by a galvanostat (Model 363, EG&G Inc., Princeton, NJ). Following anodic etching, wafer is washed with copious amount of deionized water, methanol (HPLC grade, Mallinckrodt Chemicals, Phillipsburg, NJ) and blow-dried with nitrogen gas. Dried wafers displayed an intense orange-red luminescence when excited with a 360 nm UV lamp.

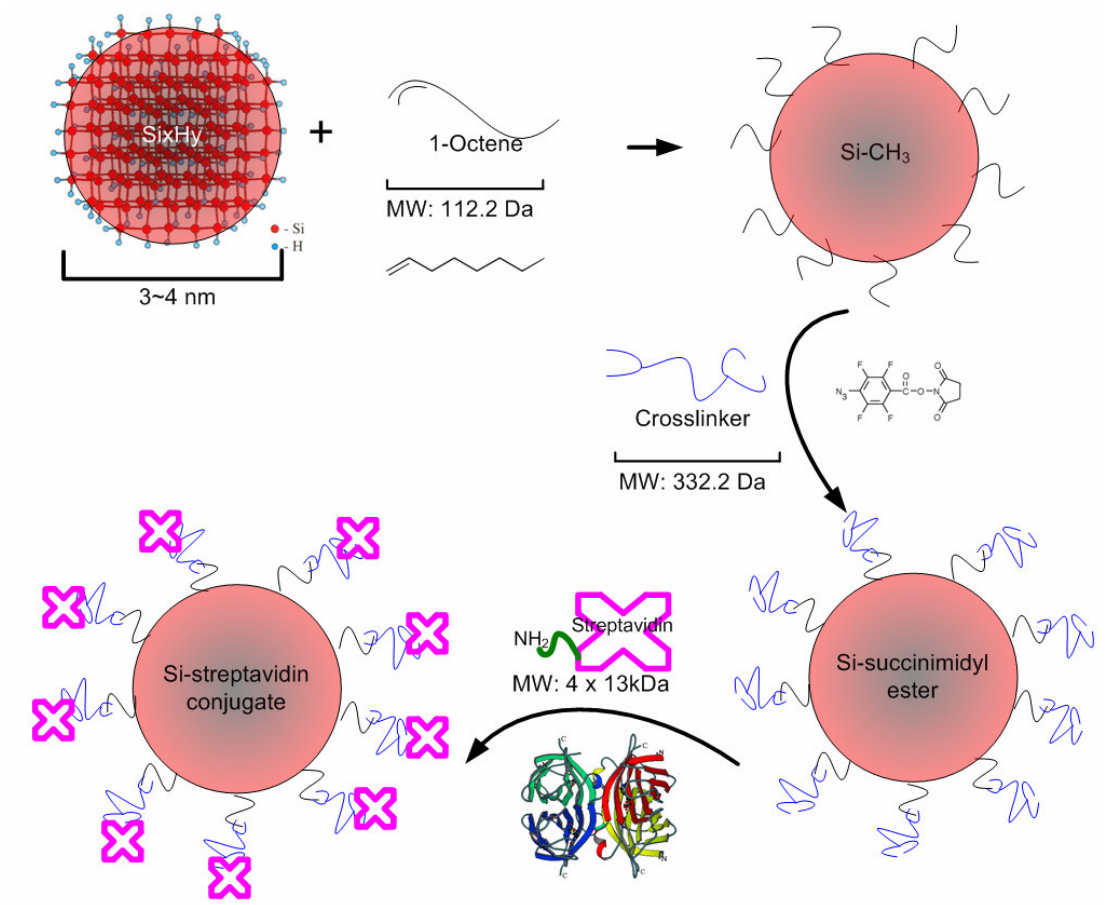

Figure 6.1 Overall schemes for functionalization and activation of Si nanocrystal and conjugation with the streptavidin.

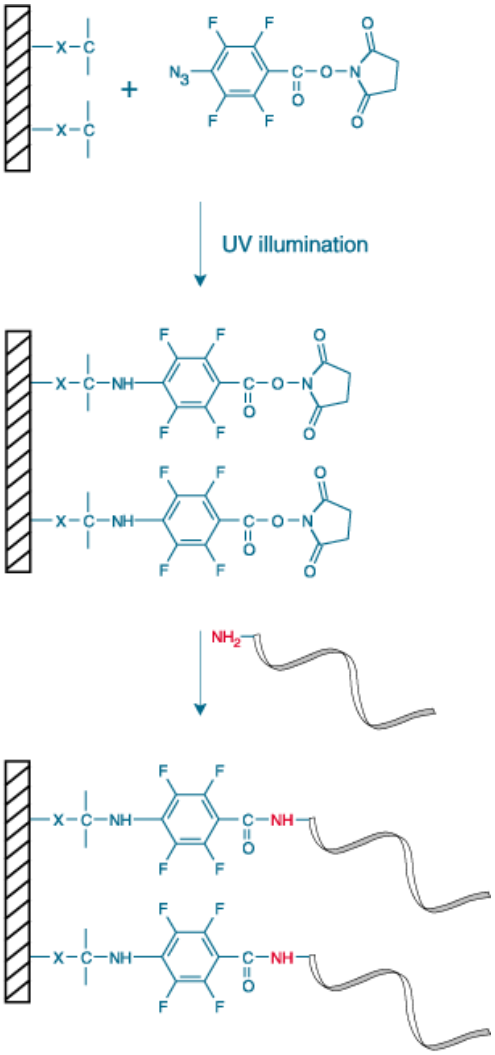

Figure 6.2 Detailed chemistry of ATFB crossliker connecting carbo-hydro terminated silicon surface to amine containing biomolecule. (Image courtesy of Invitrogen, CA)

Next, Si wafers were sonicated (Ultrasonik, York, PA) in deaerated 10:1(v:v) mixture of toluene for two hours under vigorous N_2 purging. Resulting suspension appeared orangish and exhibited weak broadband PL under UV excitation.

6.3.2 Surface activation of Si nanocrystal

After sonication, 20 ml of the Si nanoparticle suspension was delivered into the qualtz cuvette (Rayonet, Connecticut) with vigorous N_2 purging and placed inside the UV reactor (RMR-600, Rayonet, Connecticut) for photo-driven alkyl termination on silicon nanoparticles. After 30 min UV reaction with 1-octene, carbo-hydro covered SNs shined in bright blue. Next, 1-octene passivated Si nanocrystal was filtered through silica gel column to remove micron-sized aggregates.

Fig 6.1 shows overall process of bioconjugation from bare silicon nanocrystals. After we collect bright blue portion from column filtering, 1-octene terminated Si nanocrystals were introduced to a vessel for crosslinking with 4-azido-2,3,5,6-tetrafluorobenzoic acid, succinimidyl ester (ATFB, SE). As shown in Fig. 6.2, the fluorinated aryl azide group on ATFB reacts with carbo hydro group on silicon nanocrystals and provides C-N bond. 1 ml of 1-octene covered Si nanocrystals were reacted with 0.2 mL of a 15 mM solution of 4-azido-2,3,5,6-tetrafluorobenzoic acid, succinimidyl ester (ATFB, SE) (Invitrogen, CA) in anhydrous carbon tetrachloride. The nanocrystals were immediately illuminated with 365 nm lamps inside the UV reactor (RMR-600, Rayonet, Connecticut) for 5 min. After reaction, carbon tetrachloride was completely evaporated with N_2 purging.

6.3.3 Protein tagging using activated Si nanocrystals

Next, succinimidyl ester terminated Si nanocrystals were redissolved in 15 μL of anhydrous DMSO for protein conjugation. 10 mg of purified streptavidin (Pierce, IL) was dissolved in 1 mL of 0.1 M sodium bicarbonate buffer to achieve a protein concentration within 5~20 mg/mL. While we stirred the streptavidin solution, succinimidyl terminated Si nanocrystal solution was slowly added. Reaction was carried out in the dark for 1 h with magnetic stirring. After reaction for 1 h, the solution was completely dried with vacuum and N_2 purging. Subsequently, the protein conjugated Si nanocrystals are redispersed in water. Gel electrophoresis was performed to separate the conjugate from unreacted labeling reagent and protein. 15 % Tris-HCl polyacrylamide gel (Bio-Rad, CA) was used in a Tris buffer solution. 1μL of conjugated Si nanocrystals and 1μL of native streptavidin as a control were introduced into each well. After 2 h native gel electrophoresis at 200 V, the gel was removed from the eluting set-up and dyed with MicrowaveBlue (Protiga, MD) for protein staining.

6.4 Results and discussion

Figure 6.3 shows gel stained with MicrowaveBlue. When I compared with neat streptavidin, Si nanocrystal conjugates have longer elution and paler bands. Gel electrophoresis was performed in a native condition where elution of the band depends on the morphological shape and the native charges of the analytes.

Therefore, Si nanocrystal conjugated protein elutes further than neat streptavidin. The spreading in the band suggests that conjugates are not mono-dispersed because starting Si nanocrystals are not.

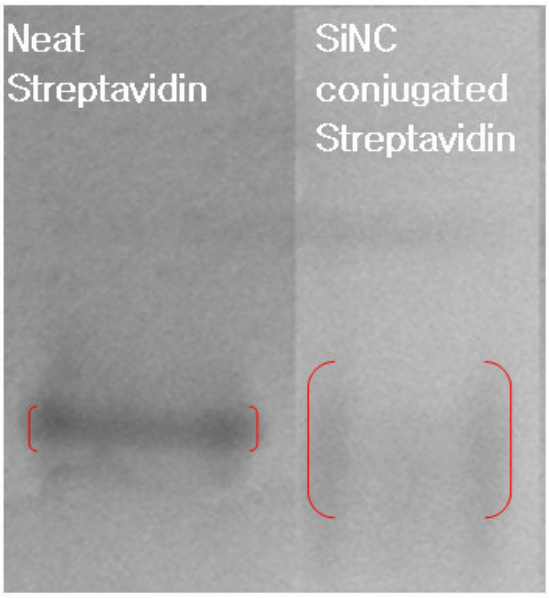

Figure 6.3 Stained gel after the native gel electrophoresis. 200V, 2 hour elution, and the mobile buffer is Tris-HCl, pH 6.8.

6.5 Summary

Streptavidin was coupled to 1-octene covered silicon nanocrystals with a bi-functional crosslinker. From native gel electrophoresis, Si nanocrystal-streptavidin conjugates are suggested to be present. Before we proceed to couple with target biomolecules (biotinylated DNA, protein etc.), we need to study bio conjugates' optical and chemical properties extensively.

6.6 References

1. Sato, S.; Swihart, M. T.; "Propionic-Acid-Terminated Silicon Nanoparticles: Synthesis and Optical Characterization", *Chem. Mater.* **2006**; *18*, 4083-4088.
2. Warner, J.H.; Hoshino, A.; Yamamoto, K.; Tilley, R.D.; "Water-Soluble Photoluminescent Silicon Quantum Dots", *Angew. Chem. Int. Ed.* **2005**, *44*, 4550-4554.
3. Hermanson, G. T. *"Bioconjugate Techniques"* **1996**, Academic Press, California.
4. Wang, L.; Reipa, V.; Blasic, J. "Silicon Nanoparticles as a Luminescent Label to DNA", *Bioconjugate Chem.* **2004**, *15*, 409-412.
5. Choi, J.; Wang, N. S.; Reipa, V.; *Langmuir*, in revision.

Chapter 7: Conclusions and Perspectives

7.1 Conclusions

7.1.1 Synthesis of Si nanocrystal

Synthesis of Si nanoparticles by the anodic etching of Si wafer and ultrasonication was successful. Wafer's fluorescence could be tuned by varying etching parameters such as the ratio of acid mixture, current density, or doping material and degree of Si wafer. However, when the nanoporous film on a surface is stripped and crumbled into particles, Si nanoparticle's fluorescence is highly affected by the type of solvent used. Among non-quenching solvents, most of the fluorescence from bare particle solution is red-orange color which means the average sizes of fluorescent particles are around 3.5~4.5 nm in diameter and they have more stable fluorescence than smaller ones.

7.1.2 Photo-assisted tuning of Si nanocrystal photoluminescence

In summary, hydrogen terminated Si nanoparticle photoluminescence wavelength and intensity can be tuned using photo-induced dissolution in HF/HNO3 acid mixture. By measuring both absorbance and photoluminescence during particle dissolution, we have tracked the Si nanoparticle band-gap growth with shrinking crystal size. Etching of Si nanoparticle methanol suspension in the HF/HNO_3 acid mixture increases PL QY up to 60%. Microsecond PL decay rates are consistent with indirect radiative recombination mechanism in particles exhibiting red to green PL. Together with high quantum yield it implies a slow nonradiative recombination and

reflect a relatively defect-free particle structure. Nanosecond decay times were recorded in Si particles with blue PL thus suggesting a direct interband transition and, possibly, a different emission mechanism. Our simple etching procedure can be employed to control particle size and prepare bright Si nanoparticle suspensions with emissions spanning the visible range, required for biological fluorescence tagging. A considerable narrowing of particle size distribution was observed during dissolution as predicted by the dissolution reaction simulation using a shrinking core model. Reaction rate dependence on particle size, predicted by our modeling was in reasonable agreement with our experimental findings. Absorbance and PL results both suggest that the median particle diameter is reduced from 5 nm to less than 1 nm, however, the smallest particles resist complete dissolution even at elevated acid concentrations. Further studies would be focused on clarifying this phenomenon and establishing optical properties with the direct size measurement of Si crystals in the sub-nanometer range.

7.1.3 Size determination of silicon nanocrystal

I studied SANS on silicon nanoparticles with mean diameters ranging from 2~5 nm. SANS yields information on size, shape and population of inorganic Si nanoparticles. HrTEM study supports the particle diameter and population deduced from SANS data. Indirect evidences of size distribution were also investigated with optical fluorescence and transmission spectra. They all confirm the size distribution of the silicon nanoparticles to be within th nanometer range determined with HrTEM and SANS. Further studies are warranted to explain relationship between the slope of

I vs. Q curve at low q region and particle's physical and chemical characteristics (shape factor, attractive or repulsive force and surface chemical compositions).

7.1.4 Surface modification of silicon nanocrystal

As predicted from theoretical studies, carbo-hydro surface modification clearly affects optical properties of silicon nanocrystals. Our experiment confirm the theoretically predicted relationship between carbo-hydro chain length and photoluminescence peak shift. Compared to H-termination, surface alkylation through UV-assisted hydrosilylation leads to higher quantum yield and significantly improves Si nanocrystal photoluminescence stability. Life time measurement suggests that blue emission after alkylation is consistent with direct radiative recombination in alkene passivated nanoparticles. From the quantum efficiency measurement,, an inverse relationship was observed between photoluminescence quantum yield and alkene chain length.

7.1.5 Bio conjugation of silicon nanocrystal

Streptavidin was coupled to 1-octene covered silicon nanocrystals with a bi-functional crosslinker. From native gel electrophoresis, Si nanocrystal-streptavidin conjugates are suggested to be present. Before we proceed to couple with target biomolecules (biotinylated DNA, protein etc.), we need to study bio conjugates' optical and chemical properties extensively.

7.2 Perspectives

In future studies, the main theme of silicon nanocrystals will be bio-conjugation and bio-tagging of DNA, and proteins. For that purpose, my research on silicon nanocrystals will focus on following points to address current shortcomings.

As a fluorescent tag, silicon nanocrystals are expected to have narrower and stronger emission peak than commercially available binary quantum dots. Therefore, the separation of silicon nanoparticles according to their sizes should be studied further for that purpose. Various approaches to separate nanoparticles such as size selective precipitation and density gradient ultracentrifugation will be tried.

For us to increase quantum yields of silicon nanocrystals, it is also required to separate bright particles from dark particles which cannot emit fluorescence.

For us to prove its superiority as a fluorescent dye, the blinking behavior of silicon nanocrystals should also be examined. If silicon nanocrystals' blinking is less severe than binary quantum dots, they will dinf many uses in biological systems.

Engineering functionality on the surface of silicon nanocrystals is another important task. The number of functional groups and percentage of coverage on each particle are important parameter to investigate.

Bio applications of silicon nanocrystals are actively on going. Pilot studies for proposing a standard reference material for DNA microarrayer are promising because of silicon nanocrystal's superior photostability against laser excitation.

Streptavidin-silicon nanocrystal conjugates will be coupled with biotin labeled biomolecules, and their tagging efficiencies and optical properties will be investigated.

An assessment of silicon nanocrystals' toxicity to cells and ultimately their utility as a fluorescent tag in living systems will be conducted by studying the uptake of silicon nanocrystal by bacteria or other cells.

Bibliography

1. Aihara, S.; Ishii, R.; Fukuhara, M.; Kamata, N.; Terunuma, D.; Hirano, Y.; Saito, N.; Aramata, M.; Kashimura, S.; "Electroreductive synthesis and optical characterization of silicon nanoparticles", *J. Non-Cryst. Sol.* **2001**, *296*, 135-138.
2. Belomoin, G.; Therrien, J.; Smith, A.; Rao, S.; Twesten, R.; Chaieb, S.; Nayfeh, M. H.; Wagner, L.; Mitas, L. "Observation of a magic discrete family of ultrabright Si nanoparticles", *Appl Phys Lett.* **2002**, *80*, 841-843.
3. Bley, R.A.; Kauzlarich, S.M.; "A Low-Temperature Solution Phase Route for the Synthesis of Silicon Nanoclusters", *J. Am. Chem. Soc.* **1996**, *118*, 12461-12462.
4. Botti, S.; Coppola, R.; Gourbilleau, F.; May, R. P.; Rizk, R.; Valli, M. "SANS and TEM investigation of laser-synthesized photoluminescent Si nanoparticles", *Appl. Phys. A* **2002**, *74*, s1230-s1232.
5. Botti, S.; Coppola, R.; May, R. P.; Valli, M. "Photoluminescence properties and size distribution in laser synthesized Si nanopowders for optoelectronic devices", *J. Appl. Cryst.* **2003**, *36*, 632-635.
6. Brasher, L. L. ; Kaler, E. W.; "A Small-Angle Neutron Scattering (SANS) Contrast Variation Investigation of Aggregate Composition in Catanionic Surfactant Mixtures", *Langmuir* **1996**, *12*, 6270-6276.
7. Brus, L.E.; Szajowski, P.F.; Wilson, W.L.; Harris, T.D.; Schuppler, S.; Citrin, P.H.; "Electronic Spectroscopy and Photophysics of Si Nanocrystals: Relationship to Bulk c-Si and Porous Si", *J. Am. Chem. Soc.* **1995**, *117*, 2915-2922.
8. Buriak, J.M.; "Organometallic Chemistry on Silicon and Germanium Surfaces", *Chem. Rev.* **2002**, *102*, 1271-1308.

9. Choi, J.; Wang, N. S.; Reipa, V.; *Langmuir*, in revision.
10. Clarke, S. J.; Hollmann C. A.; Zhang, Z.; Suffern, D.; Bradforth, S. E.; Dimitrijevic, N. M.; Minarik, W. G.; Nadeau, J. L. "Photophysics of dopamine-modified quantum dots and effects on biological systems", *Nature Materials* **2006**, *5*, 409-417.
11. Credo, G.M.; Mason, M.D.; Buratto, S.K.; "External quantum efficiency of single porous silicon nanoparticles", *Appl. Phys. Lett.* **1999**, *74*, 1978-1980.
12. Cullis, A. G.; Canham, L. T.; Calcott, D. J.; "The structural and luminescence properties of porous silicon", *J. Appl. Phys.* **1997**, *82*, 909-965.
13. Ding, z.; Quinn, M. B.; Haram, A. K.; Pell, L. E.; Korgel, B. A.; Bard, A. L. "Electrochemistry and Electrogenerated Chemiluminescence from Silicon Nanocrystal Quantum Dots", *Science* **2002**, *296*, 1293-1297.
14. English, D. S.; Pell, L. E.; Yu, Z.; Barbara, P. F.; Korgel, B. A. "Size Tunable Visible Luminescence from Individual Organic Monolayer Stabilized Silicon Nanocrystal Quantum Dots" *Nanoletters* **2002**, *2*, 681-685.
15. Fogler, H. S. *Elements of chemical reaction engineering* **2005**, 3rd ed, Prentice-Hall, New Jersey.
16. Fonseca, L.F.; Resto, O.; Gupta, S.; Katiyar, R.S.; Weisz, S.Z. *Proc. Of the 24th ICPS* **1999**, D. Gershoni ed., World Scientific.
17. Glinka, C. J.; Barker, J. G.; Hammouda, B.; Krueger, S.; Moyer, J. J.; Orts, W. J. "The 30 m Small-Angle Neutron Scattering Instruments at the National Institute of Standards and Technology", *J. Appl. Cryst.* **1998**, *31*, 430-445.
18. Haremza, J. M.; Hahn, M. A.; Krauss, T. D.; Chen, S.; Calcines, J. "Attachment

of Single CdSe Nanocrystals to Individual Single-Walled Carbon Nanotubes", *Nano Lett.* **2002**, *2*, 1253-1258.

19. Heath, J.R.; "A Liquid-Solution-Phase Synthesis of Crystalline Silicon", *Science* **1992**, *258*, 1131-1133.
20. Hermanson, G. T. *"Bioconjugate Techniques"* **1996**, Academic Press, California.
21. Hua, F.J.; Erogbogbo, F.; Swihart, M.T.; Ruckenstein, E.;"Organically Capped Silicon Nanoparticles with Blue Photoluminescence Prepared by Hydrosilylation Followed by Oxidation" *Langmuir* **2006**, *22*, 4363-4370.
22. Hua, F.; Swihart, M. T.; Ruckenstein, E. "Efficient Surface Grafting of Luminescent Silicon Quantum Dots by Photoinitiated Hydrosilylation", *Langmuir* **2005**, *21*, 6054-6062.
23. Hubbard, F. P, Jr.; Santonicola G.; Kaler, E. W.; Abbott, N. L. "Small-Angle Neutron Scattering from Mixtures of Sodium Dodecyl Sulfate and a Cationic, Bolaform Surfactant Containing Azobenzene", *Langmuir* **2005**, 21, 6131-6136.
24. Imamoglu, A.; Awschalom, D. D.; Burkard, G.; DiVincenzo, D. P.; Loss, D.; Sherwin, M.; Small, A. "Quantum Information Processing Using Quantum Dot Spins and Cavity QED", *Phys. Rev. Lett.* **1999***, 83*, 4204-4207.
25. Innerlohinger, J.; Wyss, H. M.; Glatter, O. "Colloidal Systems with Attractive Interactions: Evaluation of Scattering Data Using the Generalized Indirect Fourier Transformation Method", *J. Phys. Chem. B* **2004**, *108*, 18149-18157.
26. Innerlohinger, J. ; Villa, M.; Baron, M.; Glatter, O. "Ultra-small-angle neutron scattering from dense micrometre-sized colloidal systems: data evaluation and comparison with static light scattering", *J. Appl. Cryst.* **2006**, *39*, 202-208.

27. Jung, K. H.; Shih, S.; Hsieh, T. Y.; Kwong, D. L.; Lin T. L. "Intense photoluminescence from laterally anodized porous Si", *Appl. Phys. Lett.* **1991**, *59*, 3264-3266.

28. Kanemitsu, Y.; "Luminescence properties of nanometer-sized Si crystallites: Core and surface states", *Phys. Rev. B.* **1994**, *49*, 16845-16848.

29. Kim, T.W.; Cho, C.H.; Kim, B. H.; Park, S. J.; "Quantum confinement effect in crystalline silicon quantum dots in silicon nitride grown using SiH_4 and NH_3", *Appl. Phys. Lett.* **2006**, *88*, 123102-123103.

30. Kline, S. R. "Reduction and analysis of SANS and USANS data using IGOR Pro", *J Appl. Cryst.* **2006**, *39*, 895-900.

31. Korberling, F.; Mews, A.; Basche, T. "Oxygen-Induced Blinking of Single CdSe Nanocrystals", *Advanced Materials* **2001**, *13*, 672-676.

32. Koyama, H.; Koshida, N. "Photo-assisted tuning of luminescence from porous silicon", *J. Appl. Phys.* **1993**, *74*, 6365-6367.

33. Larson, D. R.; Zipfel, W. R.; Williams, R. M.; Clark, S. W.; Bruchez, M. P.; Wise, F. W.; Webb, W. W.; "Water-Soluble Quantum Dots for Multiphoton Fluorescence Imaging in Vivo", *Science* **2003**, *300*, 1434-1436.

34. Li, X.; He, Y.; Talukdar, S. S.; Swihart, M. T. "Process for Preparing Macroscopic Quantities of Brightly Photoluminescent Silicon Nanoparticles with Emission Spanning the Visible Spectrum", *Langmuir*, **2003**, *19*, 8490-8496.

35. Medintz, I. L; Uyeda, H. T.; Goldman E. R.; Mattoussi H. "Quantum dot bioconjugates for imaging, labelling and sensing", *Nature Materials* **2005**, *4*, 435-446.

36. Michalet, X.; Pinaud, F.F.; Bentolila, L.A.; Tsay, J.M.; Doose, S.; Li, J.J.; Sundaresan, G.; Wu, A.M.; Gambhir, S.S.; Weiss, S.; "Quantum Dots for Live Cells, in Vivo Imaging, and Diagnostics", *Science* **2005**, *307*, 538-544.

37. Mizuno, H.; Koyama, H.; Koshida, N. "Oxide-free blue photoluminescence from photochemically etched porous silicon", *Appl. Phys. Lett*. **1996**, *69*, 3779-3781.

38. Okada, R.; Iijima, S.; "Oxidation property of silicon small particles", *Appl. Phys. Lett.* **1991**, 58, 1662-1663.

39. Parker, C. A. *Photoluminescence of solutions* **1968**, Elsevier publishing company, Amsterdam.

40. Reboredo, F.A.; Galli, G.; "Theory of Alkyl-Terminated Silicon Quantum Dots", *J. Phys. Chem. B.* **2005**, *109*, 1072-1078.

41. Redl, F. X.; Cho, K. S.; Murray, C. B.; O'Brien, S. "Three-dimensional binary superlattices of magnetic nanocrystals and semiconductor quantum dots", *Nature* **2003**, *423***,** 968-971.

42. Roe, R. *Methods of X-Ray and Neutron Scattering in Polymer Science* **2000**, Oxford University Press, New York.

43. Rogozhina, E.V.; Eckhoff, D.A.; Gratton, E.; Braun, P.V.; "Carboxyl functionalization of ultrasmall luminescent silicon nanoparticles through thermal hydrosilylation", *J. Mater. Chem.* **2006**, *16*, 1421-1430.

44. Sato, S.; Swihart, M. T.; "Propionic-Acid-Terminated Silicon Nanoparticles: Synthesis and Optical Characterization", *Chem. Mater.* **2006**; *18*, 4083-4088.

45. Seraphin, A. A.; Werwa, E.; Kolenbrander, K. D. “Influence of nanostructure size on the luminescence behavior of silicon nanoparticle thin films”, *J. Mater. Res.,* **1997**, *12*, 3386-3392.

46. Skőld, K.; Price, D. L. *Methods of Experminetal Physics: Neutron Scattering* **1987**, 23, part C, Academic Press, Florida.

47. Sun, B.; Marx, E.; Greenham, N. C. “Photovoltaic Devices Using Blends of Branched CdSe Nanoparticles and Conjugated Polymers”, *Nano Lett.* **2003**, *3*, 961-963.

48. Steinert, M.; Acker, J.; Henßge, A.; Wetzig, K. “Experimental Studies on the Mechanism of Wet Chemical Etching of Silicon in HF/HNO_3 Mixtures”, *J. Electrochem. Soc*. **2005**, *152*, C843-C850.

49. Trindade, T.; O’Brien, P.; Pickett, N.L.; “Nanocrystalline Semiconductors: Synthesis, Properties, and Perspectives”, *Chem. Mater.* **2001**, *13*, 3843-3858.

50. Uhlir, A.; *Bell Syst. Tech. J.* “Electrolytic shaping of germanium and silicon”, **1956**, *35*, 333-347.

51. Wang, L.; Reipa, V.; Blasic, J. “Silicon Nanoparticles as a Luminescent Label to DNA”, *Bioconjugate Chem.* **2004**, *15*, 409-412.

52. Warner, J.H.; Hoshino, A.; Yamamoto, K.; Tilley, R.D.; “Water-Soluble Photoluminescent Silicon Quantum Dots”, *Angew. Chem. Int. Ed.* **2005**, *44*, 4550-4554.

53. Watt, A.; Thomsen, E.; Meredith, P.; Rubinsztein-Dunlop, H. “A new approach to the synthesis of conjugated polymer–nanocrystal composites for heterojunction optoelectronics”, *Chem. Commun.* **2004,** 2334-2335.

54. Wilcoxon, J.P.; Samara, G.A.; Provencio, P.N.; "Optical and electronic properties of Si nanoclusters synthesized in inverse micelles", *Phys. Rev. B.* **1999**, *60*, 2704-2714.

55. Wilson, W.L.; Szajowski, P.F.; Brus, L.E.; "Quantum Confinement in Size-Selected, Surface-Oxidized Silicon Nanocrystals", *Science* **1993**, *262*, 1242-1244.

56. Wolkin, M.V.; Jorne, J.; Fauchet, P.M.; Allan, G.; Delerue, C.; "Electronic States and Luminescence in Porous Silicon Quantum Dots: The Role of Oxygen", *Phys. Rev. Lett.* **1999**, *82*, 197-200.

57. Yamani, Z.; Ashhab, S.; Nayfeh, A.; Thompson, W. H.; Nayfeh, M. "Red to green rainbow photoluminescence from unoxidized silicon nanocrystallites", *J. Appl. Phys.* **1998**, *83*, 3929-3931.

58. Yao, J.; Larson, D. R.; Vishwasrao, H. D.; Zipfel, W. R.; Webb W. W.; "Blinking and nonradiant dark fraction of water-soluble quantum dots in aqueous solution", *Proc. of Nat. Aca. of Sci. of USA* **2005**, *102*, 14284-14289.

59. Zhou, Z.Y.; Brus, L.; Friesner, R.; "Electronic Structure and Luminescence of 1.1- and 1.4-nm Silicon Nanocrystals: Oxide Shell versus Hydrogen Passivation", *Nano Letters* **2006**, *3*, 163-167.

60. http://www.ncnr.nist.gov/programs/sans/data/data_red.html.